(54)

Characterization of a High-Current Tandem Accelerator and the Associated Development of a Water-Cooled Beryllium Target for the Production of Intense Neutron Beams

by

Brandon William Blackburn

Submitted to the Department of Nuclear Engineering in partial fulfillment of the requirements for the degree of

Master of Science

at the

MASSACHUSETTS INSTITUTE OF TECHNOLOGY

January 1997

Author.....
Department of Nuclear Engineering
January 17, 1997

Certified by.....
Professor Jacquelyn C. Yanch
Thesis Supervisor

Read by.....
Dr. Robert E. Klinkowstein
Thesis Reader

Accepted by.....
Jeffrey Freidberg
Chairman, Departmental Committee on Graduate Students

Characterization of a High-Current Tandem Accelerator and the Associated Development of a Water-Cooled Beryllium Target for the Production of Intense Neutron Beams

by

Brandon William Blackburn

Submitted to the Department of Nuclear Engineering
January 1997, in partial fulfillment of the
requirements for the degree of
Master of Science

Abstract

A tandem electrostatic accelerator capable of generating charged particle beams at currents up to 4 mA and energies up to 4.1 MeV has been built and characterized at MIT's Labaratory for Accelerator Beam Applications (LABA). Testing of the accelerator is currently underway, and the operating characteristics and design innovations have been reported. In order to produce the neutron fluence necessary for use in Boron Neutron Capture Therapy (BNCT) heat loads greater than 10 kW must be removed from the target. Submerged jet-impingement cooling has been tested in order to remove heat at fluences approaching 6 kW/cm^2. A 17 mm diameter (0.67") jet of water impinging normally on a target has effectively removed 5.07 kW/cm^2 with a heat transfer coefficient of around 2.5 W/m^2 K. It has been shown that results from this experiment can be extrapolated to higher velocity and higher Reynolds number flow. It is predicted that flow of 35 m/s can remove 6.33 kW/cm^2. Heat removal of this magnitude indicates that beryllium can be used as a target material for a 2.5 mA proton beam at 4 MeV to deliver 15 RBE-Gy to a tumor at a depth of 6 cm in 60 minutes. 15-40 RBE-Gy is deliverable to a tumor up to 4 cm in depth in a time of 40-115 minutes. Experiments conducted under both low power, low flow rate and high power, high flow rate conditions are detailed and presented.

Thesis Supervisor: Jacquelyn C. Yanch
Title: Professor, Nuclear Engineering

Thesis Reader: Robert E. Klinkowstein

Acknowledgments

For the past year I have had the great pleasure of working for Professor Jacquelyn Yanch in the Department of Nuclear Engineering. Her leadership and guidance has been invaluable in allowing me to complete my work. Rarely have I met a professor who not only will work hard at their own research but will also take the time to be your friend. In all the time I worked for her, she never once hesitated when I asked her for anything, and she was always willing to go the extra step to make sure that all the members of the group were on track. At one point in the year, I lost the use of my car for a period of three weeks. When I first told Professor Yanch about the situation, she immediately offered that I could use her car if I needed. I do not think she realized how much that meant to me. That instance typifies the helpfulness and friendship that she showed to me from the moment I started with the group. I appreciate everything she has done, and I can honestly say that had it not been for Professor Yanch, I would not have accomplished what I have at MIT.

My family will always be at the top of any list when it comes to people I have to thank. In what was a trying and difficult year at times, my parents were always a foundation on which I could rely for strength and encouragement. Their love and patience have never wavered toward me, and I thank them for that. It would take an additional thesis to list all that they have done for me. Mom and dad, I thank you and love you always. Skoo and K.P, you guys are the best. You always supported me, and I thank you for your love. Kelly, Stacy, and P.T, your calls and letters of encouragement were exactly what I needed when times were tough. To all my family, I could never adequately thank you for what you mean to me.

Haijun Song, Bill Howard, and Emanuela Binello have been great teammates and friends during my time in the LABA group. Were it not for Bill and Haijun, I would not be as skilled in moving and plumbing as I am. Bill has always provided a strong sense of leadership to the LABA group and has always been willing to help. I owe Haijun a great deal of thanks for the many weekends and late nights he spent helping me move and get my stuff ready.

I want to thank Bob Klinkowstein and Ruth Shefer of NSI in helping me with many of my projects over the year. Were it not for Bob, I doubt that I would have been able to do any of my experiments. Your guidance and insight into design and experimentation have been incredible. Much of the practical hands-on learning that I have gained at MIT is due to Bob's help and instruction. I also want to thank Ruth for helping me with my papers and posters. She always knew how to say what I wanted to say, and she could always make it sound just right.

Of all the friends I have met this past year, no one means more to me than Denise. She is the best friend anyone could have, and had it not been for her, I don't know how I would have made it in Boston. There were many calls late at night during rough times, and Loobey was always there for me. She never complained, always gave of herself, and never expected anything in return. There are many others with whom I have spent time both at work and at play over the past year. Many of these people have become good friends and have supported me throughout the year. Mark, Kathleen, Rob, Dave, Randy, I will always remember you guys.

No acknowledgment would be complete without giving thanks to God, who makes all things possible. I know that it is only by His faithfulness that I have been able to make it. All honor is His.

-Brandon W. Blackburn

Table of Contents

Appendix

References

List of Figures

List of Tables

Chapter 1

INTRODUCTION AND CONTRIBUTIONS OF THIS WORK

1.1 Introduction

Since the 1950's, Boron Neutron Capture Therapy (BNCT) has been investigated as a means by which the uptake of a boronated compound in the desired cell, followed by irradiation with thermal neutrons could be used to treat various forms of melanoma and brain tumors. Recent work carried out at MIT has also adapted this modality to the treatment of arthritis in a process known as Boron Neutron Capture Synovectomy (BNCS).

Although most previous work in the area of BNCT has, to this date, been carried out using a reactor as the neutron source, a high-current tandem accelerator for use in research has been constructed and is being tested at MIT's Laboratory for Accelerator Beam Applications (LABA). BNCT research has focused on the use of epithermal neutrons for the treatment of various tumors. Epithermal neutrons have enough energy to penetrate tumors located deep within the brain. After being absorbed by boronated compounds in the tumor, the neutron initiates the $^{10}B(n,\alpha)^{7}Li$ reaction. The ranges of the lithium and alpha particles are on the order of microns, allowing the energy of the reaction to be absorbed almost entirely by the boron-loaded cells. Conventional production of the

high neutron flux needed for BNCT experiments has been provided by a nuclear reactor. Innovations in technology, however, have made feasible the use of an accelerator to produce intense neutron beams. Cost, size, and dose considerations for the accelerator make it an attractive alternative to a reactor. The tandem accelerator being tested has been designed to produce multi-milliampere proton or deuteron beams with a maximum energy of 4.1 MeV. Design innovations include a high output multicusp negative-ion source, magnetic suppression of secondary particles to reduce background radiation, and a switch-mode-type high voltage generator [1].

Two major concerns with the use of an accelerator for the production of neutrons for BNCT involve (1) the ability to produce sufficient multi-milliampere charged particle beams of several MeV and (2) an effective means by which tens of kilowatts of power can be removed from a neutron producing target. This thesis addresses both of these concerns; greater emphasis is placed on the second in an attempt to answer the question of whether or not a target can be constructed which can feasibly remove high heat loads.

1.2 Goals of this Thesis

Chapter 2 of this thesis provides a summary of the operating mechanisms of the new LABA accelerator, and can serve as a reference and a working description of the innovative new accelerator design.

Based on concerns regarding the target design and its ability to remove large heat loads, investigations targeted the cooling capabilities of a high velocity submerged water jet. According to neutron production requirements which will be specified in later

chapters, it was desired that the target be able to handle heat loads on the order of 6 kW/ cm^2. At this level, a target with a surface area of 10-20 cm^2 could easily handle the required beam power needed for BNCT. Beyond the quantification of its cooling ability, it was desired that the target design be simple yet durable. Instead of designing a complex target with cooling channels or fins that require a great deal of machining, a simple beryllium disk was used which made the construction of the target simple yet effective. This simplicity is important when considering the viability of this modalitity as a clinical procedure.

1.3 Contributions of this Work

The first contribution of this work is to outline and characterize the operation of the new LABA accelerator which was designed by Newton Scientific Inc. (NSI) of Cambridge, MA. Innovations in its design make possible the generation of up to 4 mA of charged particles at energies up to 4.1 MeV.

In regards to the design of a high-power beryllium target, the submerged jet impingement design was tested up to levels in excess of 5 kW/cm^2 with a flow velocity of 24.13 m/s which was supplied by a 15 HP centrifugal pump. At this level, the heat transfer coefficient for the target was found to be 2.5×10^5 W/m^2 K. Effective heat removal of this magnitude from beryllium allows the delivery of 15 RBE-Gy to a tumor at a 6 cm depth in 60 minutes using a 2.5 mA beam at 4 MeV, and 15-40 RBE-Gy to a tumor at a depth of up to 4 cm in 40-115 min [2].

Finally, it was shown that a simple yet effective target could be built and cooled with minimal machining and construction. The design used in this target had no moving parts and required little machining, which viewed in the light of the toxicity of beryllium, makes this a very attractive alternative.

1.4 Outline of Thesis

The first section of the thesis deals with the characterization of the new LABA accelerator. Chapter 2 provides a detailed description of the operation and a number of the innovations incorporated into the NSI design.

Chapter 3 provides details on the heat transfer fundamentals which will be used to explain the capabilities of the submerged jet impingement cooling. Using the fundamentals explained in Chapter 3, Chapter 4 expands the fundamentals into the actual design of the target tested during this research.

Details of the experiments are presented in Chapter 5, while the results and conclusions are given in Chapters 6 and 7 respectively.

Chapter 2

THE TANDEM ACCELERATOR AT MIT-LABA

2.1 Layout of the LABA Accelerator Facility

The accelerator which will be described in the following sections was constructed in about one year and is located in a laboratory in the basement of a building at the Massachusetts Institute of Technology (MIT). Layout of the accelerator room, vault, control room, and adjoining areas is shown in Figure 2.1.1. The lab room measures approximately 17' x 38' and houses the accelerator, the power supplies for all components, as well as the first sections of the exterior beam line and a beam steering magnet. The walls and ceiling of the facility are constructed of concrete and standard building materials. Experiments are carried out in a radiation vault which is connected to the accelerator lab with a 44" thick concrete wall. A small port in the wall is used to pass a beam line from the lab into the vault. During experimentation, this area around the beam line is filled with shielding material such as boronated polyethylene. Control of the accelerator is provided by computers located in a control room which is separated from the vault by a three foot thick concrete wall and two foot thick door.

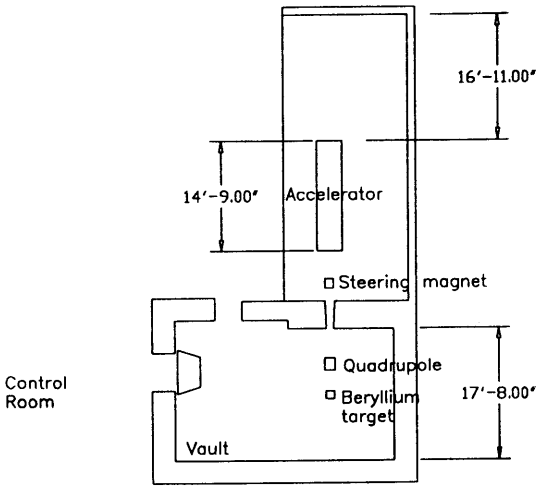

Figure 2.1.1 Layout of the accelerator and various experiments at MIT-LABA.

2.2 High Voltage Accelerators

Tandem accelerators belong to the larger more general class of electrostatic linear accelerators. Machines of this type accelerate charged particles in a linear fashion utilizing an electrostatic high-voltage generator. Conventional electrostatic accelerators produce positively charged ions within the high-voltage terminal and are then accelerated toward the ground potential. The final energy of the particle is simply the product of the voltage of the terminal (V_0) and the charge of each particle (q). Under this configuration, the ion source and the initial acceleration and focusing components must be confined within the high-voltage terminal.

Tandem, or multi-stage accelerators, are different in that the acceleration occurs in two or more separate stages. In models of this type, a high-voltage electrostatic field is placed on a terminal somewhere along the accelerating structure as opposed to the end. The tandem accelerator constructed by NSI in conjunction with the LABA is a two-stage

tandem accelerator. In a two-stage tandem, a beam of negative ions is first produced by an ion-source and injected into the first section of the accelerating column. These particles experience an attractive force and are accelerated toward the high voltage terminal. For example, H^- ions accelerated toward a terminal at 1 MV would acquire a kinetic energy of 1 MeV. These ions must be converted into positively charged particles before they can pass through the second stage of acceleration. Conversion is accomplished either by passing the negative ions through a gas or through a stripping foil. Upon passing through the stripping foil, electrons are removed and a positive ion is produced. The positive ion is again accelerated away from the high voltage terminal towards ground potential. Thus, upon exiting the accelerating column, the particle has gained a kinetic energy equal to twice the product of the terminal voltage and the charge on the ion ($2qV_0$).

2.3 Physical Description of the Accelerator

An advantage that the tandem accelerator has over a reactor based neutron source is its compact size. A nuclear reactor facility requires a large space on the order of tens of meters as well as a large containment building. In contrast, the LABA accelerator can be located in a room (5-10 m^2) which is easily incorporated into an existing hospital or facility. Figure 2.3.1 illustrates the completed accelerator and associated power supplies.

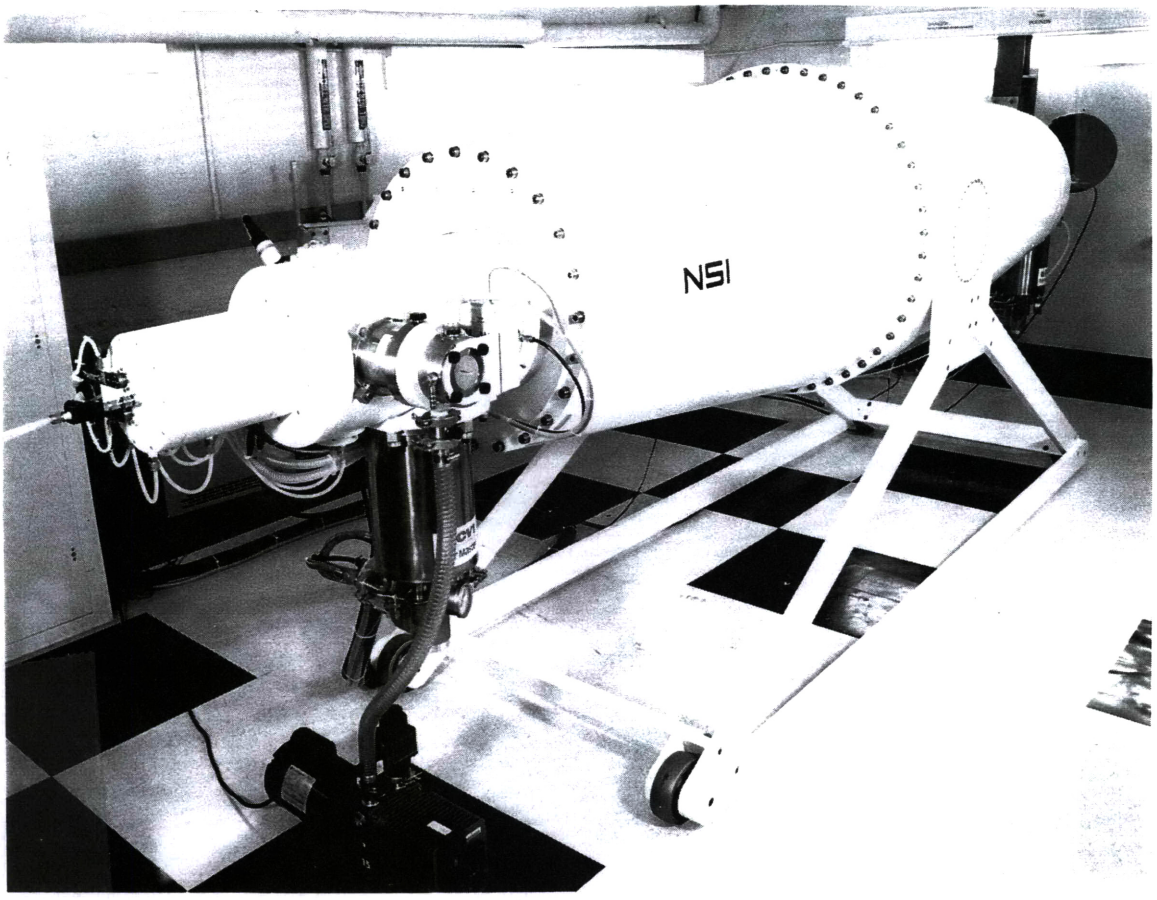

Figure 2.3.1 Photograph of the completed accelerator with the associated power supplies.

Three main components comprise the working body of the accelerator and are shown in Figure 2.3.2. Listed in the order in which ions are produced and accelerated toward the target, these components are: (1) the ion-source, (2) the injector, (3) the accelerating column and pressure vessel. Taken collectively these components have a combined weight of nearly 1000 kg. The length of the entire machine from the end of the ion source to the end of the pressure vessel is 3.9m. The largest diameter achieved by the truncated cones which make up the pressure vessel is 0.94 m. Supported by an adjustable aluminum stand which can be moved on rollers, the accelerator has a height of 1.6 m at the highest point on the pressure vessel.

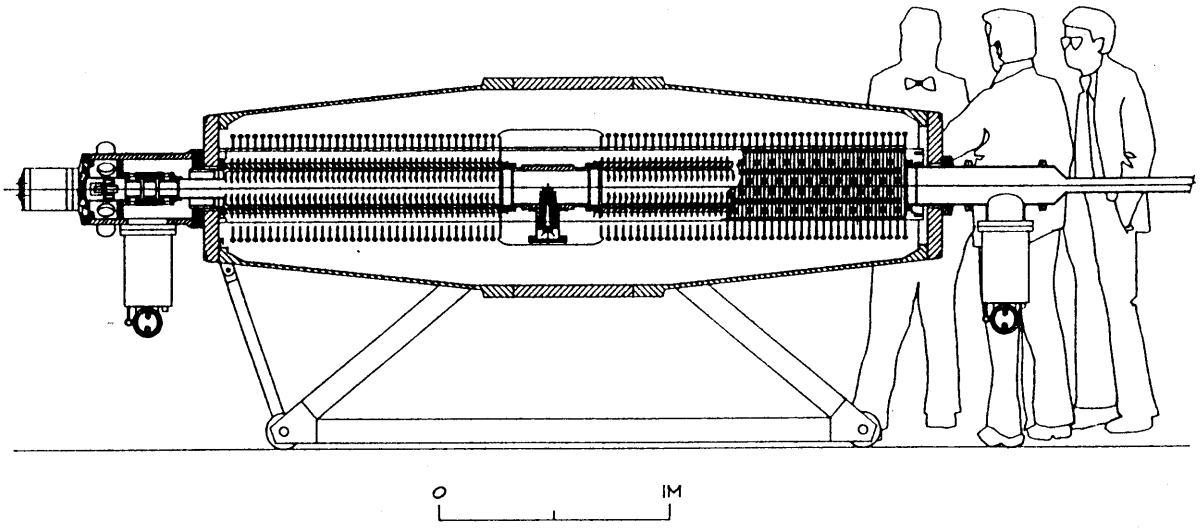

Figure 2.3.2 Schematic of the accelerator illustrating the main working components.

2.4 Basic Tandem Accelerator Operation

LABA's tandem electrostatic accelerator is designed to accelerate up to 4 mA of protons or deuterons and achieve energies of up to 4.1 MeV in order to produce neutrons via the $^{7}Li(p,n)^{7}Be$, $^{9}Be(p,n)^{9}B$, or the other charged particle reactions. The following is a basic description of the accelerator operation. Figure 2.4.1 illustrates the separate components as they are oriented within the body of the accelerator. Further details will be provided in later sections. First, negative ions are produced by a high-current multicusp source. These ions are extracted at 3 keV and then accelerated to 20 keV as they enter the injector which incorporates two-orthogonal Wein filters, X-Y steering plates, and an Einzel lens. Before entering the low energy accelerating tube, the ions are also focused by the fringe fields of the tube itself. Once inside the low-energy tube, the negative ions are accelerated toward the high-voltage terminal. High voltage is supplied to the terminal by means of a

high-frequency switch-mode converter coupled to a solid state cascade voltage multiplier circuit [3]. The ions are stripped of their electrons in the terminal by passing them through a carbon stripping foil mounted on a stainless-steel holder. Final acceleration occurs in the second accelerating tube as the now positive ions are accelerated toward ground potential.

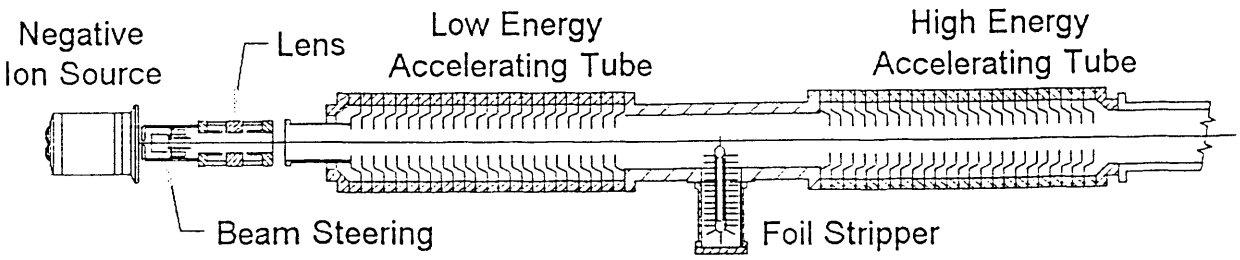

Figure 2.4.1 Orientation of accelerator components within the main body of accelerator.

Several innovative technologies have been incorporated into the accelerator making it feasible to produce the required current at energies which can be used in BNCT research. The energy of the beam is continuously tunable over the range of 0.5-4.1 MeV. This fact could be exploited in the investigation of near-threshold reactions of a variety of neutron-producing targets. In addition, the ion-source and the target structure are at ground potential outside of the pressure vessel. With this orientation, changes to the ion-source or modification of the target and neutron moderator are greatly simplified. No invasion into the pressure vessel or accelerating column is needed to make changes to the target or moderator. Additional innovations which will be described in the subsequent sections include magnetic suppression of secondary radiation, the high-current multicusp

negative ion source, and the switch-mode type high voltage generator. The following sections will describe the individual working of each of the major components of the accelerator. For clarity, the order in which they are described follows the progression of the ions through the accelerator from production to exit.

2.5 High-Current Multicusp Negative Ion-Source

Conventional negative ion sources used in tandem accelerators, such as duoplasmatrons or sputter sources, are unable to provide negative ion currents which are sufficient for neutron production for BNCT. Maximum outputs of these types of sources is limited to currents of less than 100μA [3]. Research in the early 1980's, however, indicated that a relatively large concentration of negative hydrogen ions were present in the volume of a hydrogen discharge [4]. Utilizing dissociative attatchment, the multicusp negative ion source, shown in Figure 2.5.1, was designed to produce up to 5 mA of H^-. The ion-source is 25.4 cm long with a diameter of 18.4 cm. It is joined to the injector with a compression flange of diameter 30.5 cm.

Production of negative ions begins with the introduction of high purity H_2 gas through the terminal block into the plasma discharge volume which has been evacuated to between 10^{-7}-10^{-8} torr by a cryogenic pump. Gas flow is facilitated through a digital flow controller which limits the input of hydrogen to a few cc/min during operation. When the gas is introduced, the pressure inside the chamber is increased to a few milli- torr.

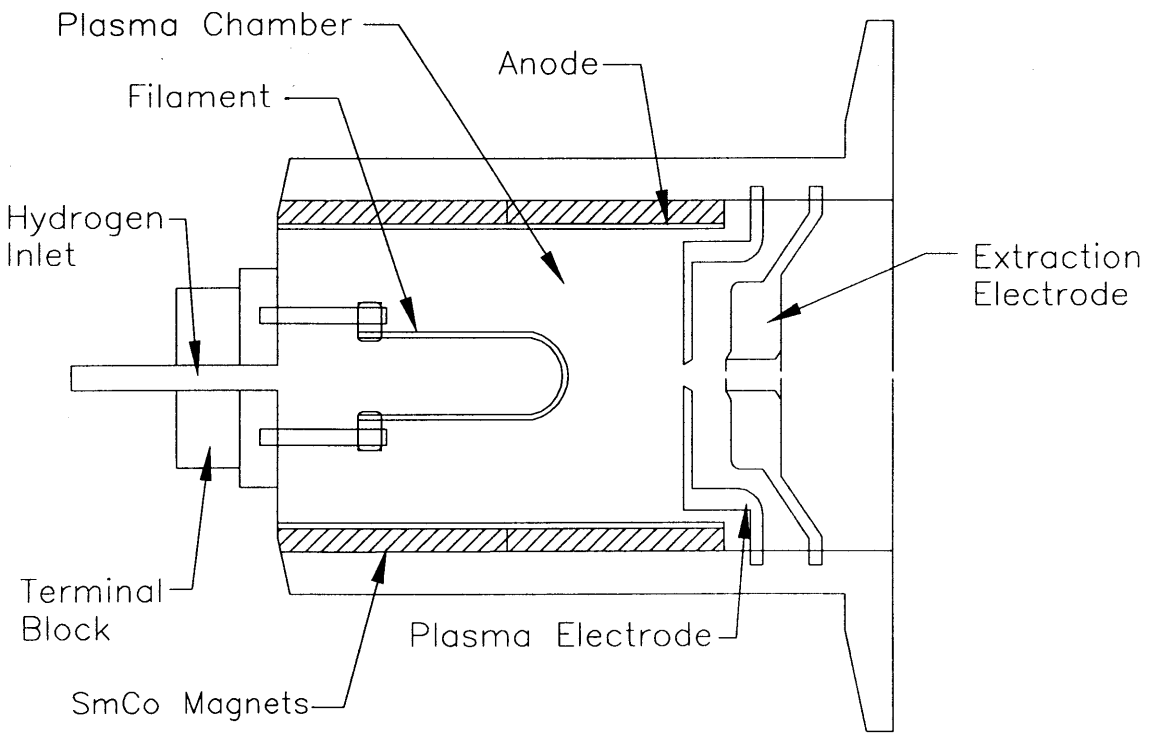

Figure 2.5.1 Schematic of multicusp ion source on LABA accelerator.

The cylindrical plasma discharge volume is separated magnetically into two regions by ten cobalt-samarium magnets placed around the edge of the water-cooled copper chamber and held in place by the magnet holder. These magnets are oriented in an anti-symmetrical fashion so that a high-order multipole field separates the volume into two regions. The first region extends from the filament end of the source to within a few millimeters of the extraction aperture. Here, high energy electrons, which are boiled off the filament and accelerated to approximately 100 eV, interact with the gas to generate vibrationally excited H_2 molecules. It is also possible that these electrons can ionize or disassociate the H_2 molecules. The resultant spectrum of electrons has a Maxwellian shape with an average temperature of approximately 2 eV.

The tungsten filament is heated to emission temperatures by passing approximately 175A through the filament itself. Once the filament reaches a temperature of 2250 °C, thermionic emission facilitates the ejection of electrons from the surface. Having been emitted, these electrons are accelerated toward the body of the chamber which serves as the anode with a bias of 100 V. Although these electrons are ejected at nearly 100 eV, they are quickly slowed by excitation and ionizing collisions. These ionizations produce a low energy thermal population of electrons which, along with the hydrogen molecules, can pass through the magnetic filter and enter the extraction chamber.

In the extraction chamber, hydrogen molecules which have been vibrationally and rotationally excited through collisions with the walls of the chamber and through collisions with energetic electrons, are in close proximity to low energy electrons with energies less than 1 eV. It is here that the fundamental process of dissociative attachment produces H^- ions. Although the discussion of the physics of dissociative attachment is beyond the scope of this investigation, references [4-6] should be investigated for further information.

The basic reactions which take place in the extraction chamber are

$$e + H_3^+ \rightarrow H^- + H_2^+ \qquad (2.5.1)$$

$$e + H_2(^3\Pi_u) \rightarrow H^- + H \qquad (2.5.2)$$

$$e + H_2(v^*) \rightarrow H^- + H \qquad (2.5.3)$$

where $H_2(^3\Pi_u)$ represents a hydrogen molecule in an excited rotational state, and $H_2(v^*)$ represents an excited vibrational state [5].

The extraction electrode draws the H^- ions out of the extraction chamber. Electrons are also drawn out of the plasma discharge along with the negative hydrogen ions by an electric field applied by the extraction electrode. In order to filter out the electrons, small magnets are located near the extraction electrode aperture. This electrode is biased to a few keV. Electrons are deflected by a transverse magnetic field of nearly 100G and collected on the extraction electrode. Experiments indicate that nearly 90% of the electrons are removed by this magnetic field while the remaining 10% strike the acceleration electrode [6]. Thus, the beam that is accelerated to nearly 20 keV by the acceleration electrode consists mainly of H^- ions. The beam, which has entered the injector as it is accelerated to 20 keV, now passes through the injector where it will be filtered and steered so that it will be directed along the axis of the accelerator.

2.6 The Injector System

Beginning from the acceleration electrode, the components which make up the injection system include two Wein filters, horizontal and vertical steering plates, and an Einzel lens. The combined effect of these components is to focus and steer the beam so that it is in the correct orientation to enter the accelerating tube. High current ion beams of low energies expand under the influence of space charge forces. This space charge effect degrades the beam quality. The injector system is designed to minimize the distance from the ion source to the entrance of the low energy accelerating tube in order to minimize the spreading effect of beam space charge [3]. Since it is possible that heavy ion contaminants will be present in the beam, mass filtering is accomplished by two Wein filters. These

filters produce perpendicular electric and magnetic fields which are transverse to beam velocity. These fields are adjusted so that for the desired species ie. protons or deuterons, the two fields will exactly cancel, and these ions will pass straight through. Unwanted heavier ions will be deflected out of the path of the beam. The Wein filters are also used to steer the H^- beam. In order to prepare the beam for injection into the accelerating tube, an Einzel lens biased to around 4.5 kV is used to focus the beam. As the beam approaches the entrance to the low energy tube, the fringe fields produce a strong focusing effect. The total length of the injector system is 0.5 m and its diameter is 30.5 cm.

2.7 Switch-Mode High Voltage Generator

A high-frequency switching power supply is used to provide power to the accelerator high-voltage terminal. The switching power supply, which can produce up to 12 kW, begins the production of high voltage by generating square wave signals at a certain voltage level and frequency. Each of the pulses are on the order of hundreds of volts while the frequency of the pulses are several kHz. Under steady state conditions, these pulses are uniform in width. The signal from the supply is then sent to a step-up transformer which is mounted on the end flange of the pressure vessel. Space is conserved through the mounting of the transformer and multiplier circuit directly to the accelerator, thereby eliminating the need for an external power chassis [7]. Voltage from the power supply is stepped up by a factor of 200 in the transformer before it is applied to the first stage of the multiplying circuit.

A modified Jones and Waters circuit is employed to produce terminal voltages of up to 2.05 MV. This circuit, which is diagrammed in Figure 2.7.1, originated in the Research Laboratories of Associated Electrical Industries Ltd. It was developed to improve upon the poor characteristics of the Cockcroft and Walton multiplying circuit [8].

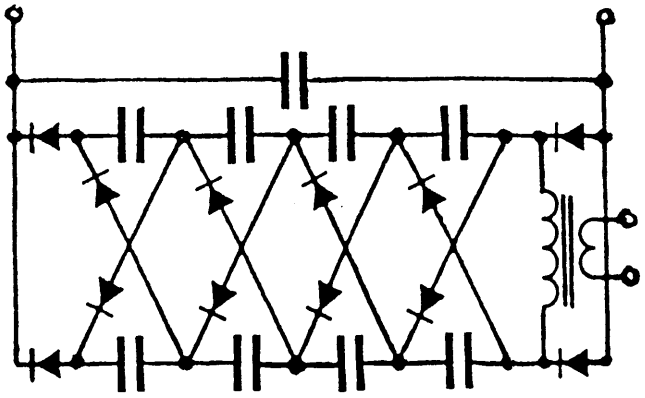

Figure 2.7.1 The modified Hones and Waters circuit employed in the LABA accelerator.

The circuit is divided into two sections which are located on the top and bottom of each stage on the high-voltage end of the accelerating column. Switching the load from the top to the bottom sections during each cycle limits the voltage ripple. In each alternate half-cycle, each capacitor except those at the very top transfer their charge to the one in the opposite stack [8]. The rectifying nature of the circuit transforms the periodic voltage pulses from the power supply into a DC signal with a very small voltage ripple. Terminal voltage is monitored by a high-voltage electric field sensor which is configured to sample the field created by the charge on the terminal. During operation, the sensor is actively

coupled to the power supply to provide feedback. When current is accelerated at increasingly higher voltages, the terminal becomes loaded, and the voltage will decrease. This decrease in voltage is detected and returned to the power supply. In response to this loading, the power supply will maintain terminal voltage by increasing the pulse width of the switching converter.

2.8 Pressure Vessel and Insulating Gas

The pressure vessel consists of two conical sections joined to a 0.94 m diameter cylinder section in the middle of the accelerator. The vessel is designed in accordance with the ASME pressure vessel code. The body of the pressure vessel is constructed of aluminum with a thickness of 1.6 cm on the conical sections of the tank while the section which covers the high-voltage terminal has a wall thickness of 5 cm. The flanges at the ends of the pressure vessel are 5 cm thick and have a diameter of 0.63 m. Attempts to charge the terminal to voltages higher that 220 kV in air are unsuccessful because of the dielectric breakdown which occurs at 30 kV/cm at 15 psia. In order to bring the terminal up to 2.05 MV, which is needed to accelerate a proton to 4.1 MeV, the accelerator must be insulated with pressurized sulfur-hexaflouride (SF_6). An empirical relation, listed as Equation 2.8.1, can be used to estimate the limiting voltage achievable under a certain pressurization with SF_6.

$$\text{Electric Field Breakdown}(SF_6) = 75\ (P/15)^{0.6}\ \text{kV/cm} \qquad (2.8.1)$$

where P is the absolute pressure of the insulating SF_6 in psi

In order to achieve terminal voltages of 2.05 MV, the vessel has been pressurized to 105 psia. Using the above relation, the point of breakdown is found to be 241 kV/cm. Thus, the insulating gas has improved the achievable voltage by a factor of seven compared with atmospheric air alone. A gas recovery system was also constructed which allows the tank to be emptied and filled without loss of all gas from the vessel. Since SF_6 is heavier than air, precautions such as monitoring oxygen levels have been instituted in the lab to protect against asphyxiation due to oxygen displacement.

2.9 Low and High Energy Accelerating Tubes

The ion beam is accelerated by a uniform electric field which is produced by two accelerating tubes mounted with the accelerating column. Aluminum electrodes and glass insulators are alternately stacked in an assembly to form each accelerating tube as shown in Figure 2.9.1.

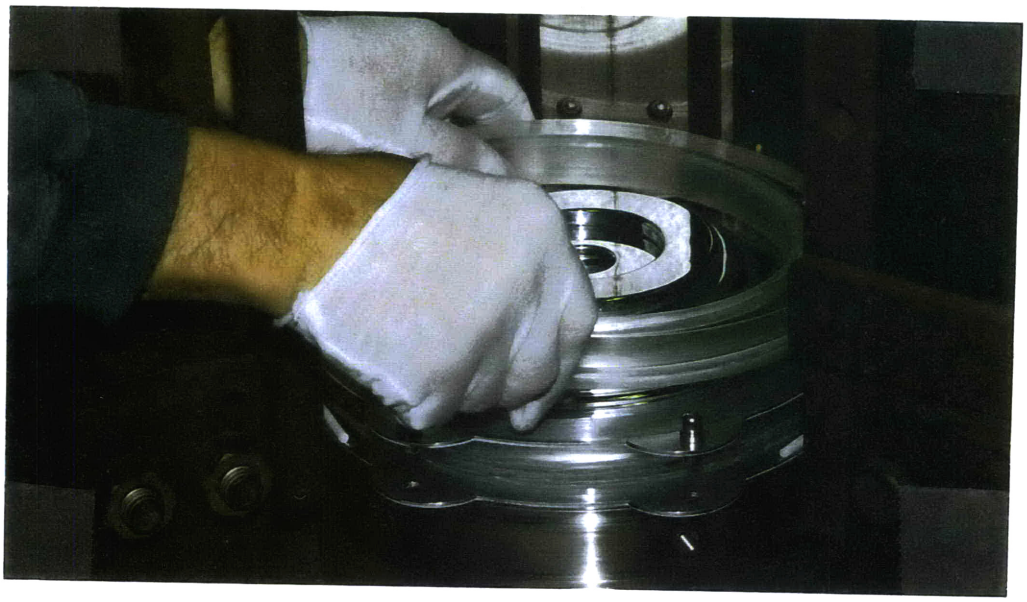

Figure 2.9.1 Photograph of electrodes and glass insulators inside accelerating column.

The accelerating tubes were manufactured by Vivirad High Voltage Corporation in Billerica, MA. To assemble the tube, the aluminum electrodes were machined with an opening for the beam as shown in Figure 2.9.2. A transverse magnetic field is applied at each electrode by a pair of samarium-cobalt magnets to suppress secondary electron production in the accelerating tube. Most tandem accelerators have used inclined electric fields to suppress secondary electron production. Although this has been used successfully at low currents, proton trajectories become unstable at high currents, which leads to an overall loss of current. Magnetic suppression is effected by two magnets positioned on each electrode by a suppression magnet holder. This holder aligns the magnets in such a way as to create a magnetic field perpendicular to the axis of the accelerator. Any electron that is produced within the accelerating tube will be turned out of the beam before it gains sufficient energy to produce energetic bremmstrahlung radiation.

Figure 2.9.2 Photograph which illustrates the suppression magnets in the electrodes.

Between each electrode is an annular glass insulator. In order to join successive sections of the tube, adhesive was applied to the glass, and the electrodes and insulators were stacked in a jig. This assembly was heated to 160 °C in order to cure the adhesive.

The low energy end of the tube is located between the injection system and the terminal. No voltage multiplication circuitry is located in this section as is the case on the high energy side which is between the terminal and the exit of the accelerator. 47 stages make up the low energy end of the tube, while 52 stages make up the high energy side. Voltage is distributed to the low and high energy accelerating tube electrodes through a simple voltage divider circuit which uses 47 and 52 200 MΩ resistors respectively to connect each of the electrodes. The resultant gradient in each of the tubes is uniform, and at a terminal voltage of 2.05 MeV the voltage gradients are 17.17 kV/cm for the low energy tube and 15.52 kV/cm for the high energy tube.

2.10 Carbon Stripping Foils

Negatively charged particles which have been accelerated to an energy qV_0 in the low energy side must be stripped of their electrons in the terminal. Two possible methods have been employed to facilitate the production of positive particles: (1) gas stripping and (2) carbon stripping foils. Gas stripping can handle large currents easily, and there is no chance of damage to the stripping medium. Ionization in the stripping gas does, however, create a secondary load on the power supply. This load can exceed that contributed by the primary beam by several times under acceleration of high current. To avoid this drawback, carbon stripping foils are incorporated in the tandem accelerator at LABA for

production of positively charged particles. These foils are extremely thin (5-10 $\mu g/cm^2$) although they strip nearly 100% of the electrons on the incoming particles. Foils are mounted on stainless steel sleeves with an openings of either 5/8 or 7/8 in. diameter. These sleeves are held on a rotating platform which can accommodate over 50 foils. Each foil has a limited lifetime depending on the thickness, beam current, and accelerating voltage. Predictions of foil lifetimes from 10-100 mA-hours have been developed for proton beam energies of 1.25-2 MeV [3].

Stripping is the final process in the creation of the charged particle beam before it enters the second accelerating region. After the beam is accelerated toward ground potential, it exits the accelerator where it can be focused and steered in order to strike a target, where it then deposits its energy. This energy is the source of heat which must be removed in order to keep the target from melting. Removal of this energy is a heat transfer process which will be developed in the following chapter.

Chapter 3

HEAT TRANSFER

3.1 Fundamentals of Heat Transfer

Heat transfer involves the movement of energy through a body resulting from a temperature gradient. Whereas thermodynamics deals with the end states of an energetic process, the intermediate processes by which heat energy is carried from one place to another and the rates at which this occurs is the domain of heat transfer. In order to understand the mechanisms of heat transfer involved in the design of a high-power accelerator target, the basics of conduction, convection, and radiation must be developed.

Perhaps the simplest form of heat transfer, conduction involves the movement of heat through a body in which there exists a temperature gradient. Conduction requires only that a temperature gradient exists in a body. If this body is a gas or liquid, the movement of the molecules gives rise to a diffusion of energy. Because the hot molecules have a greater velocity than the colder molecules, there will be a net movement of heat from a hot region towards a colder region. In a solid, this transfer occurs in much the same way although there are differences in the mechanisms of conductors and insulators. In conductors the vibration of free electrons and thermal waves within the atomic lattice allows for heat transfer, while insulators allow only lattice waves. Correspondingly, there

is a very strong correlation between the electrical conductivity and thermal conductivity of materials.

Conduction can be expressed as a rate equation known as Fourier's Law. This equation states that the heat flux per unit area is proportional to both the thermal conductance of a material and the temperature gradient. A negative sign indicates that heat always travels from a hot to cold regions.

$$q'' = -k\, dt/dx \qquad (3.1.1)$$

$$q = -A\, k\, dt/dx \qquad (3.1.2)$$

where

q": heat flux (W/m^2)

k: thermal conductivity (W/m K)

q: heat (W)

A: area of body perpendicular to heat flow (m^2)

dt/dx: temperature gradient per unit length (K/m)

While conduction will occur in any body independent of motion, convection involves both the diffusion of heat and the bulk motion of a fluid. If a surface is in contact with a fluid which is at a lower temperature, any movement of the fluid will remove heat from the interface. If this fluid motion is due to flow resulting from an external forcing mechanism such as a pump, it is referred to as forced convection. Free convection occurs when temperature gradients in the fluid create density gradients. As the fluid moves due

to the buoyancy forces, the fluid motion gives rise to free or natural convection. As a rule, forced convection is more efficient than free convection at removing heat. Fluid motion can also be induced by boiling or condensation. Convection involving a phase change is even more effective than forced convection. Jet impingement cooling, a subset of convection, will be investigated in greater detail later in the chapter.

Convection is illustrated by Newton's Law of Cooling which states that the heat flux due to convection is proportional to a constant (h) and the temperature gradient between the surface and the fluid.

$$q'' = h\,(T_f - T_s) \tag{3.1.3}$$

$$q = h\,A\,(T_f - T_s) \tag{3.1.4}$$

where h: convective heat transfer coefficient ($W/m^2\,K$)

T_f: fluid temperature (K)

T_s: surface temperature (K)

Determination of the heat transfer coefficient will be the primary task of experiments in a convective system. Once h has been determined, the performance of a cooling system can be predicted. In order to determine an experimental value for h, three primary properties of the fluid must be determined. These properties are: temperature, conductivity, and velocity. For most applications, the heat transfer coefficient will be most strongly coupled

with fluid velocity. If a phase change is occurring, the latent heat becomes important in determining h. The definition of h will be provided in section 3.2.

Radiation is the only heat transfer mechanism which requires no medium in which to take place. The movement of heat is carried out by electromagnetic radiation primarily in the visible and infra-red energies. In most applications radiation becomes important only at high temperatures or in the presence of a vacuum. According to the Stefan-Boltzman Law, radiative heat transfer can be expressed by:

$$q'' = \varepsilon \sigma (T_s^4 - T_\infty^4) \qquad (3.1.5)$$

where

ε: emissivity of the surface

σ: Stefan-Boltzman constant
5.67×10^{-8} W / m2 K4

T_∞: temperature of surroundings (K)

3.2 Convection

Most heat transfer applications make use of a moving fluid in order to carry away heat from a surface. As indicated by Equation 3.1.3, the coefficient h must be determined before the heat transfer capacity of a system can be predicted. Calculation of this coefficient is central to the study of heat transfer. Many well-known relationships exist which provide expressions for calculating h under certain conditions. As a rule, these expressions are good for specific flow geometries within a range of flow parameters. These expressions commonly have the form:

$$Nu = \text{Constant } Re^{a} Pr^{b} \qquad (3.2.1)$$

where Nu: Nusselt Number

Re: Reynolds Number

Pr: Prandtl Number

Parameters such as the Nusselt, Reynolds, and Prandtl Number are non-dimensional relations which are dependent on various coolant properties.

The Nusselt Number is a ratio of the convective to conductive heat transfer in the cooling fluid at the surface boundary. A value of unity indicates that the fluid is stagnant and conducting only. As Nu increases, the convection of the fluid improves. Nu can be expressed as:

$$Nu = h\,d / k \qquad (3.2.2)$$

where d: characteristic length or diameter

k: conduction coefficient of fluid

In applications such as jet impingement cooling, d would be the diameter of the jet nozzle.

The Reynolds Number (Re) is simply a ratio of the inertial and viscous forces in a moving fluid and can be expressed by:

$$Re = V\,d\,/\,\nu \qquad (3.2.3)$$

where V: fluid velocity (m/s)

ν: kinematic viscosity (m^2/s)

The final parameter, Prandtl Number (Pr), is the ratio of momentum and thermal diffusivity. It simply indicates the ability of a fluid to transport energy and momentum in the thermal and velocity boundary layers [9]. Although this value can be calculated from inherent fluid properties it is simply a constant dependent only on temperature.

3.3 Determination of h

The determination of h is specific to each geometry and flow pattern. It is also important to realize that relations such as 3.2.1 are typically good over a very specific range of Re and Pr. Although approximations for h can be developed by using Nusselt Number relations derived for similar situations, in order to accurately determine the heat transfer capability of a system, h must be found for each system. Standard experiments for determining h are done as follows:

(1) Configure the heat transfer system and flow pattern.

(2) Evaluate the power (q) placed on target.

(3) Measure the temperature of the flow or jet in order to determine fluid properties.

(4) Determine the velocity of the flow or jet in order to calculate Re.

(5) Determine the surface temperature of the target (T_s).

(6) Calculate the area A through which the heat is being transferred.

(7) Use 3.1.4 to determine h.

Once h has been determined for a range of Re and Pr, an expression in the form of 3.2.1 can be developed. This expression can now be used to predict the heat transfer capability of a similar system within a defined flow regime.

3.4 Boiling Heat Transfer

When a surface covered in liquid becomes hot enough to raise the temperature to the point where the fluid's vapor pressure is equal to or greater than the surrounding pressure, boiling will occur. This point occurs if T_s exceeds the saturation temperature (T_{sat}) of the fluid. This temperature excess (T_e) is given by $T_s - T_{sat}$, where T_{sat} is a function only of pressure for a specific liquid. Even before boiling begins, heat is being transferred away from the surface due to the enhanced natural convection of the water. Once boiling begins, however, heat transfer is greatly enhanced due to the utilization of the latent heat of vaporization in the boiling process. Pool boiling, which is simply boiling in a stagnant body of water, can dissipate up to 10^6 W/m^2 before a departure from nucleate boiling (DNB) occurs.

Departure from nucleate boiling occurs when the heat flux from the surface exceeds that which can be adequately handled by boiling. When this occurs, a layer of

vapor blankets the heated surface, and the heat transfer falls by orders of magnitude. The point at which this occurs is termed the critical heat flux (CHF). If a significant amount of heat is being deposited in the target when DNB occurs, the target can and will heat up quickly past the point of failure. In many instances, failure is immediate and catastrophic. The critical heat flux has been measured for pool boiling and is given in the expression [9]:

$$q''_{max} = 0.149 h_{fg} \rho_v \left[\frac{\sigma g (\rho_l - \rho_v)}{\rho_v^2} \right]^{1/4} \tag{3.4.1}$$

where h_{fg}: heat of vaporization (J / kg)

ρ_v: density of vapor (kg / m^3)

ρ_l: density of liquid (kg / m^3)

σ: surface tension (N / m)

The above expression holds for a heated surface covered in a layer of stagnant fluid. For water at 1 atm, CHF occurs when the heat flux exceeds 1.29 MW/ m^2. If this fluid is forced across the surface of the target, the added heat transfer from the convection will raise the point of CHF past that of pool boiling. Furthermore, if the flow is configured so that the dynamic pressure on the heated surface is greater than atmospheric pressure, the saturation point of the fluid will be increased thereby raising the point of CHF. Jet impingement cooling is perhaps the most effective way to take advantage of all these mechanisms in order to transfer heat away from a surface.

3.5 Jet Impingement Cooling

The use of submerged impinging jets has been studied as a means of enhanced heat transfer in electronic devices, industrial processes, and as an innovative target cooling mechanism. Under similar heating and coolant conditions, jet impingement is the most effective flow mechanism for the enhancement of heat transfer. In addition, experimental evidence suggests that submerged jet impingement is 25% more effective in removing heat than with free surface impingement [10]. Using a submerged high velocity jet of water confined in a test assembly, power densities of up to 6 kW/cm^2 have been dissipated with heat transfer coefficients of 10^6 W/m^2 K. Table 3.5.1 indicates relative ranges of various types of heat transfer coefficients.

Submerged jet impingement involves the injection of an axisymmetric flow of fluid by means of a nozzle through a region of the same fluid at rest above the target. The jet entrains fluid from the stationary body as it strikes the target. Upon striking the target surface, the jet spreads out radially from the area of impact which is termed the stagnation point. This radial spreading combined with the entrainment of the fluid above the target, keeps the jet at a lower temperature than with forced convection. The fact that a phase change can also occur allows the removal of heat through the vaporization of the coolant. This use of boiling substantially improves the effectiveness of submerged jet impingement, but it is extremely important that CHF not be exceeded when boiling occurs.

Table 3.5.1. Ranges of Various Heat Transfer Coefficients [9]

Mechanism	**Coefficient range (W/m^2 K)**
Free liquid convection	50-1000
Forced liquid convection	50-20000
Radiation at 1600 K	10^{-4}-10^5
Convection with phase change	2500-10^5
Submerged jet with phase change	>6x10^5

In jet impingement studies, in addition to parameters such as Re and Pr, certain non-dimensional parameters must also be specified. These are given as ratios in terms the nozzle diameter.

Z/d: nozzle to target spacing

r/d: radial distance from stagnation point

A/d: target size

Non-dimensional parameters such as Z/D can be altered by changing the size of the nozzle and by adjusting its position relative to the target.

The fundamentals of heat transfer and the method for evaluating the heat transfer coefficient which were presented in this chapter, served as a the foundation for the design of the high power target which will be detailed in the following chapter.

Chapter 4

TARGET DESIGN AND THEORETICAL CALCULATIONS

4.1 Introduction to Target Design

Development of Accelerator Based Boron Neutron Capture Therapy (BNCT) as a viable clinical procedure depends on the reliability, compact-nature, and cost effectiveness of an accelerator to produce an intense source of neutrons. In order to achieve neutron production on the order of 10^{10}-10^{12} n/s, low Z metals such as ^{7}Li or ^{9}Be can be bombarded with multi-milliampere beams of either protons or deuterons at energies of a few MeV. At these energies, heavy charged particles will be completely stopped within millimeters or less of the target material, thereby requiring that powers of several kilowatts be removed. Beryllium was chosen as a target material for initial investigation because of its thermal, mechanical, chemical, and neutron producing characteristics. This chapter investigates the potential of submerged water jet impingement as a means of removing in excess of 10 kW from a neutron producing beryllium target. Design considerations and theoretical calculations performed during the development of the high-power target are presented. Figure 4.1.1 and 4.1.2 should be referenced while reading the following sections. These figures and photographs illustrate the target that was designed for the heat transfer experiments.

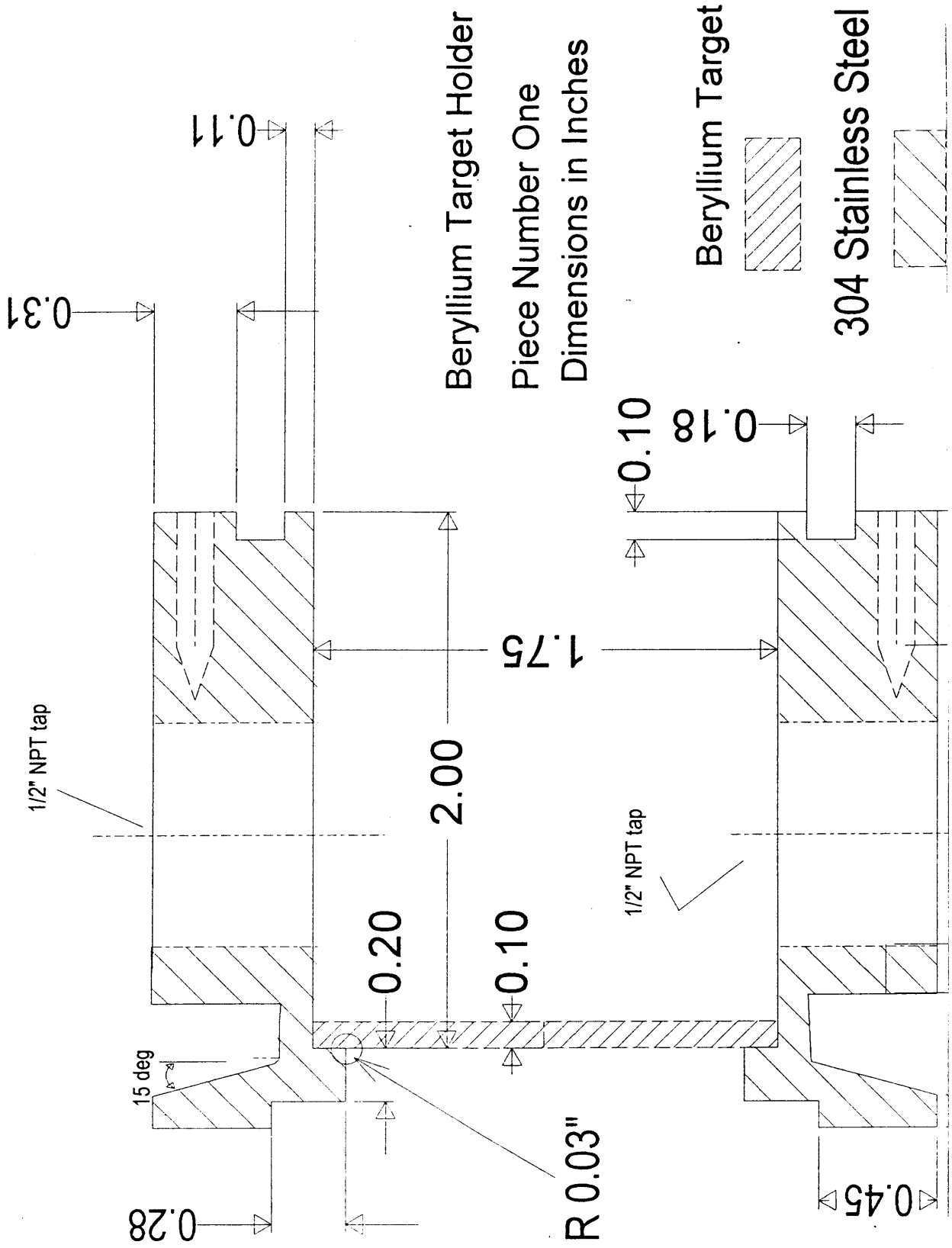

Figure 4.1.1 Mechanical diagram of beryllium target designed to test heat transfer.

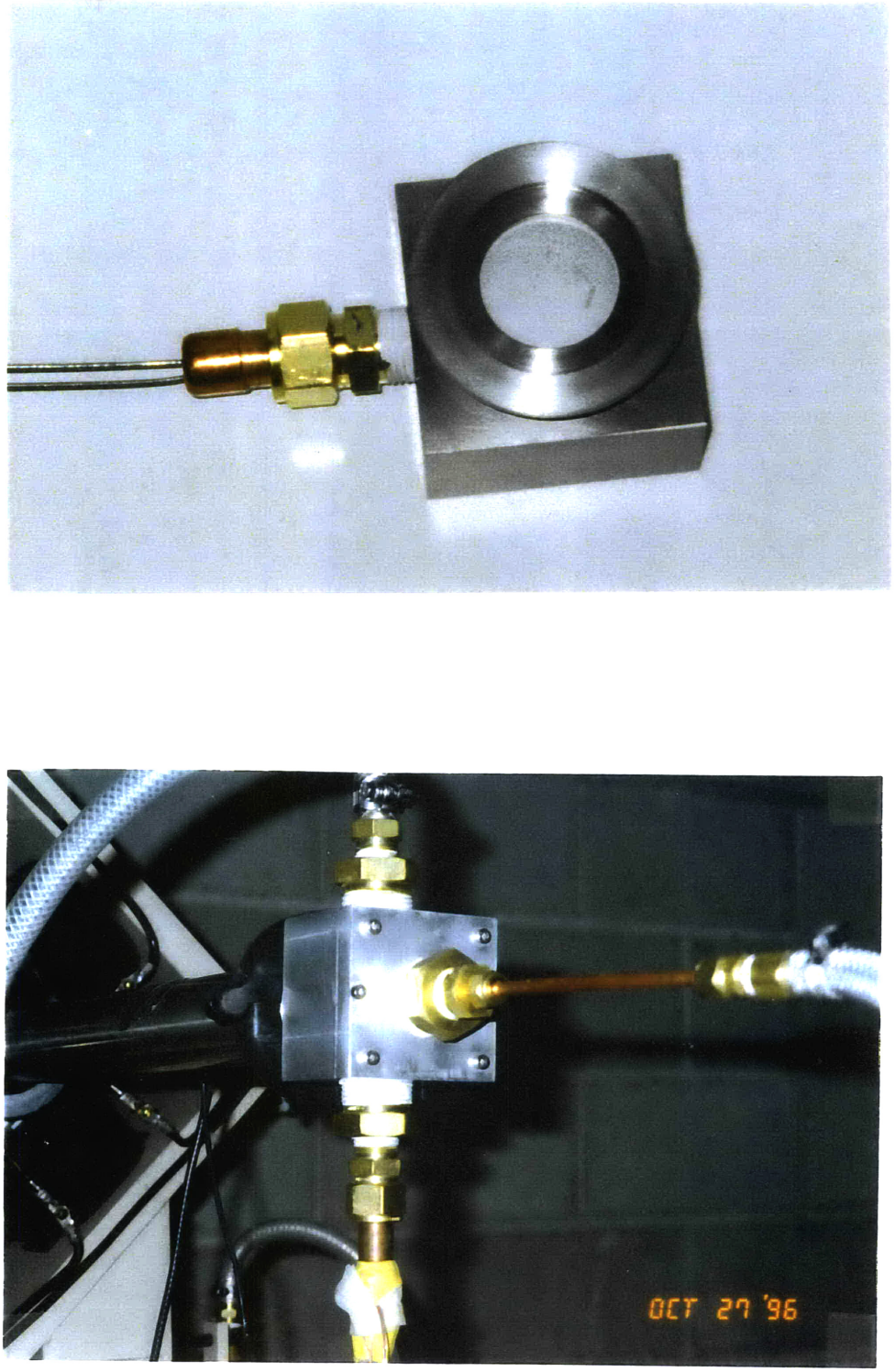

Figure 4.1.2 Photographs of beryllium target.

4.2 Target Requirements for BNCT

Production of neutrons can be accomplished by bombarding a low Z material such as lithium or beryllium with protons or deuterons. Example yields are shown below in Table 4.2.1.

Table 4.2.1 Some typical neutron producing reactions proposed for BNCT [2].

REACTION	OUTPUT	BEAM ENERGY
$^{7}Li(p,n)^{7}Be$	$8.97x10^{11}$n/s-mA	2.5 MeV
$^{9}Be(p,n)^{9}B$	$5.25x10^{11}$n/s-mA	4 MeV
$^{9}Be(d,n)^{10}B$	$1.0x10^{12}$n/s-mA	2.6 MeV

For each reaction, it is estimated that currents between 2.5-4 mA will be needed in order to make therapy times reasonable [2]. This translates into as much as 10-16 kW of power that must be removed from the target. If the beam is spread over a 15 cm^2 area, the power density would be around 1 kW/cm^2. Normally, however, the beam is made to cover an area of approximately one-half the total target area making the local power densities on the order of 2 kW/cm^2. Removal of heat fluences on the order of 2 kW/cm^2 is difficult with forced convection, even when a phase change of the coolant is utilized. Rrelations developed by Eichhorn and Lienhard [11] for forced convection with a phase change indicates that even with a flow of 35 m/s across a tube with a diameter of 0.87" only 1.5 kW/cm^2 can be removed. In order to design a practical target that can be used for BNCT, a more effective means of heat transfer must be incorporated. Also, the target

material must be able to withstand high heat loads while maintaining good thermal conductivity.

4.3 Target Material Properties

The two most promising target materials from a neutronic standpoint are lithium and beryllium. Lithium, in fact, is the better choice neutronically because the energy spectrum of the emitted neutrons is softer thereby requiring less moderation. It fails to be a good target choice from a thermal and mechanical standpoint. Table 4.3.1 indicates the relevant thermal and mechanical properties of beryllium and lithium.

Table 4.3.1 Mechanical and thermal properties of typical BNCT target materials [12].

	Melting Point (°C)	Conductivity (W/m K)	Yield Strength (Pa)
Beryllium	1286	210	260×10^6
Lithium	180.5	84.7	small

Interestingly, beryllium maintains a large yield strength at high temperatures. Even at temperatures in excess of 600 °C, the yield strength is approximately 100 MPa [13].

Lithium is not only a poor thermal conductor, but its explosive reactivity with water makes engineering of a cooling system which uses water as the working fluid difficult. Because of its poor conduction, use of lithium targets has typically been limited to lithium oxides or thin layers deposited on a copper substrate. These targets are disadvantageous because not only do they replace a large mass fraction of lithium with

other non-neutron producing elements, but they also suffer from significant sputtering effects when bombarded by energetic beams.

Because of its strength, conductivity, and neutron producing capability, beryllium was chosen as the target material for the high-power target. The one difficulty that is encountered with the beryllium target is the machining. The dust of beryllium is extremely toxic, and machining can only be carried out by certified individuals. All machining for this target was carried out by Brush-Wellman.

4.4 Target Radius and Thickness

There are two basic requirements for the size of the target. The first is that its radius and thickness should be large enough so that a beam can be spread over as much of the available area as possible providing that the entire beam strikes the target without scraping the beam tube. The second is that the target be mechanically sound even under extreme operating conditions. It was noted earlier that up to 16 kW of power could ultimately be deposited on the target. In order to provide a large target surface area, the beryllium was constructed with a diameter of 1.75" resulting in an area of 15.52 cm^2. Conveniently, this diameter is slightly less than the 1.85" ID of a standard KF-50 flange.

The thickness of the target is dependent on the pressure that will be exerted on the target, and the range of the bombarding particles. For a beam of 4.1 MeV, heavy charged particles have a range of between 10-20 mils. The pressure considerations, therefore, were the main criteria for choosing a target thickness. In order to calculate the thickness needed, the following relation from [14] was used.

$$S = 0.25(E\, p^2\, a^2 / t^2)^{1/3} \qquad (4.4.1)$$

where: S: maximum stress on the target (psi)

E: Young's Modulus (psi)

p: pressure (psi)

a: radius of target (in.)

t: thickness of target (in.)

Considering a beryllium target at 650 °C with a 1.75" diameter under vacuum and being struck on one side with a jet of water at 35 m/s, the thickness needed was calculated to be 0.76". This is an extremely conservative measurement since the tensile strength of beryllium is as much as a factor of two higher at operating temperatures of a few hundred degrees Celsius [13]. Under normal operation of the target, the beryllium would be held at only a few hundred degrees Celsius. The only time that the target might approach 650 °C, would be under extreme heat loads of several kW/cm^2. For an added measure of safety, the target was designed with a thickness of 0.1"

4.5 Target Design Considerations

Taking advantage of the simplicity and efficiency of jet impingement cooling, the high-power target was designed to have a single jet strike the back of the target at high velocity

in order to remove the heat. From the beginning, the target was designed to remove up to 6 kW/cm^2. With a target area of 15.5 cm^2, the ≈90 kW that could be removed from the target, would be more than sufficient for BNCT.

Two primary references were consulted in order to serve as a basis for the high-power design. A Soviet experiment by Maceika and Skema indicated that heat fluxes as high as 6 kW/cm^2 had been dissipated by a 18 mm diameter submerged nozzle at a cooling flow rate of 35.3 m/s [15]. Results from these experiments also suggested that the optimum diameter for the cooling nozzle was ½ that of the area being cooled. The target, therefore, was designed to allow nozzles of various diameters (0.1-0.87") to be tested.

The second reference by Garimella and Rice indicated that the optimum Z/D spacing would be found typically between 1-5 [16]. In fact, all experiments conducted by Garimella and Rice and in this work indicated that the optimum Z/D spacing was normally 1. Reasoning for this conclusion is that it is desirable for the potential core to strike the target after it is well developed. Past a Z/D of 5, the core has begun to deteriorate, whereas before 1 Z/D the core is still suffering from nozzle exit effects.

4.6 Target Cooling Estimations

As mentioned in Chapter 3, boiling can serve to increase the convective heat transfer coefficient. For target design, however, it is necessary that the point of CHF be known since any type of burnout while on the accelerator would have catastrophic results. For the target constructed in this work, the following calculations were used to estimate the point of CHF.

One of the most basic estimates of the heat removing capabilities of water is a control volume calculation. A control volume cconsiders only the energy entering a specified volume and the energy leaving. The difference in the amount that enters and leaves must be deposited or generated in the control volume. For this example, radiative losses have been neglected due to the low temperature of the target. Using the control volume approach:

$$q_{max} = m\, c_p\, \Delta T_{coolant} \tag{4.6.1}$$

where m: mass flow rate (kg/s)

c_p: specific heat (J/kg ^{o}C)

$\Delta T_{coolant}$: temperature rise in cooling fluid

For a relatively large beam which covers the majority of the target, the heat flux (W/m^2 K) is simply

$$q'' = q / A_{target} \tag{4.6.2}$$

The same argument can be used to relate the temperature increase in the coolant to the temperature distribution in the target wall. Under steady state

$$m\, c_p\, \Delta T_{coolant} = (A_{target}\, k_{Al}\, \Delta T_{wall}) / \Delta X_{wall} \tag{4.6.3}$$

where ΔT_{wall}: temperature difference from front to back

ΔX_{wall}: wall thickness

Although Eq. 4.6.1 seems to indicate that the heat capacity of water would allow the dissipation of many kilowatts of power with only minimal temperature increase, a competing effect limits this ability. As the temperature of the target goes above the saturation temperature for water, nucleate boiling begins to occur. This boiling is desirable because the latent heat of vaporization increases the achievable convective heat transfer coefficient. As the target surface in contact with the water continues to increase above the saturation point, the temperature excess causes a region of vapor to be deposited on the target. Normally, the velocity of the jet is sufficient to sweep away this vapor layer in order to keep liquid water in contact with the target. Once the heat flux becomes so high that the vapor bubbles cannot be moved away from the surface, the vapor layer sharply decreases the heat transfer and causes the temperature of the target to rise dramatically. The amount of heat needed to cause this phenomenon is known as the critical heat flux (CHF). The departure from nucleate boiling is thought to be the cause of failure for targets subjected to high thermal loads. Failure for targets that exceed the critical heat flux occurs rapidly with catastrophic results. Therefore, careful monitoring of the target temperature should be maintained so that any deviations from the expected temperature increase can be used as a warning of pending failure.

A well know relation for the maximum heat flux in a saturated body of fluid is

$$q''max_{sat} = 0.149 h_{fg} \rho_v \left[\frac{\sigma g(\rho_l - \rho_v)}{\rho_v^{21}} \right]^{0.25} \quad (4.6.4)$$

where h_{fg}: heat of vaporization at saturation (kJ/kg)

r_v: vapor density at saturation (kg/m^3)

r_l: liquid density at saturation (kg/m^3)

s: surface tension (N/m)

For stagnant saturated water at atmospheric pressure, the critical heat flux is found to be 0.129 kW/cm^2. Usually, however, the fluid used in cooling a target is kept below the saturation temperature. This sub-cooling increases the point of critical heat flux and can be estimated by [15]

$$qmax''_{sub\text{-}cooled} = q''max_{sat} \left[1 + 0.112 \left(\frac{\rho_l}{\rho_v} \right)^{0.8} \left(\frac{c_p \Delta T_{sub}}{h_{fg}} \right)^{1.13} \right] \quad (4.6.5)$$

where ΔT_{sub}: degree of subcooling below saturation

With water at 25°C, the critical heat flux becomes 0.680 kW/cm^2. This improvement of more than a factor of 5 means that heat transfer is more efficient with a colder working fluid. Critical heat flux in a jet impingement configuration also depends on the velocity of the coolant.

The greater the velocity of the coolant, the more momentum is available in the jet to sweep away the vapor bubbles from the surface. Tests performed by Maceika and Skema

at velocities of up to 35.3 m/s in a nozzle with a 1.8 cm diameter and heat fluxes approaching 6 kW/cm^2, provide the experimental data which indicate a dependence on fluid velocity of the form

$$q''max = qmax''_{sub\text{-}cooled} [1+0.92\ v_f^{0.44}] \qquad (4.6.6)$$

4.7 Comparisons of Aluminum and Stainless Targets

In order to conduct actual tests of the target, an identical target was built with the actual target surface constructed of aluminum instead of beryllium. This was necessary to test the target without the production of the associated neutron radiation. Aluminum was chosen because its conductivity (237 W/ m K) is very close to that of beryllium.

For high power tests which were also conducted it was necessary to replace the aluminum with thin stainless steel target. Stainless steel has a poor thermal conductivity which is nearly 15-20 times less than beryllium [9]. Results gained from stainless steel would normally be improved when using a beryllium target.

Because of the properties of the two different target materials used in the experiments, the following experiments, which are described in the following chapter, can be used to establish the effectiveness of the heat transfer capabilities of the target whose design was presented in this chapter.

Chapter 5

EXPERIMENTAL SETUP AND PROCEDURES

5.1 Introduction

In section 3.3, seven steps for determining the heat transfer coefficient (h) were outlined. It is the purpose of this chapter to describe the setup and the experimental procedures which were followed to determine the heat transfer capability of the target. As detailed in the previous chapter, the beryllium target was replaced during these experiments in order to test the heat removal without production of the associated neutron radiation. Where possible, an identical aluminum target was used because of its similar heat conduction coefficient.

Heat transfer experiments were carried out by two different methods which will be described in the following sections. The primary difference in the experiments involved the power source. For the first set of experiments, power was placed on target using the LABA accelerator for which the target will ultimately be used, and experiments were performed at heating levels of up to 475 W. The second set of experiments were conducted on a separate power supply capable of producing up to 48 kW of power.

5.2 Low Power Tests on the Accelerator

Initial tests using, the accelerator were conducted using an aluminum target identical to that described in Chapter 4. Testing of this target was conducted using proton beams with powers up to 475 W and coolant flow rates of up to 1.5 GPM. It was decided that power levels would be kept low in order stay well below the calculated CHF value.

5.2.1 Configuring the cooling system

The first step in testing the target was the construction of the cooling system illustrated in Figure 5.2.1. Cooling water was provided by a Barnstead/Thermolyne model D4521 deionizing system. From the cooling system, the piping was split into two parallel lines in order to decrease the friction losses. Using 1/2" plastic tubing, the water was brought from the accelerator room to the vault area through the radiation port in the wall, which divides the two rooms. Tubing was then connected to two Omega FL-215 shielded rotameters which were used to determine the flow rate. By using two high precision needle-valves connected just prior to the flowmeters, up to 6 LPM ($\approx$ 1.5 GPM) could be measured with an accuracy of $\pm$ 5%. Connections from each of the flowmeters were joined into a single line which were connected to the target through the port on the back of the target housing. Water exited the top of the housing through a single port before being split into two parrallel return lines which transported the cooling water back to the deionization system.

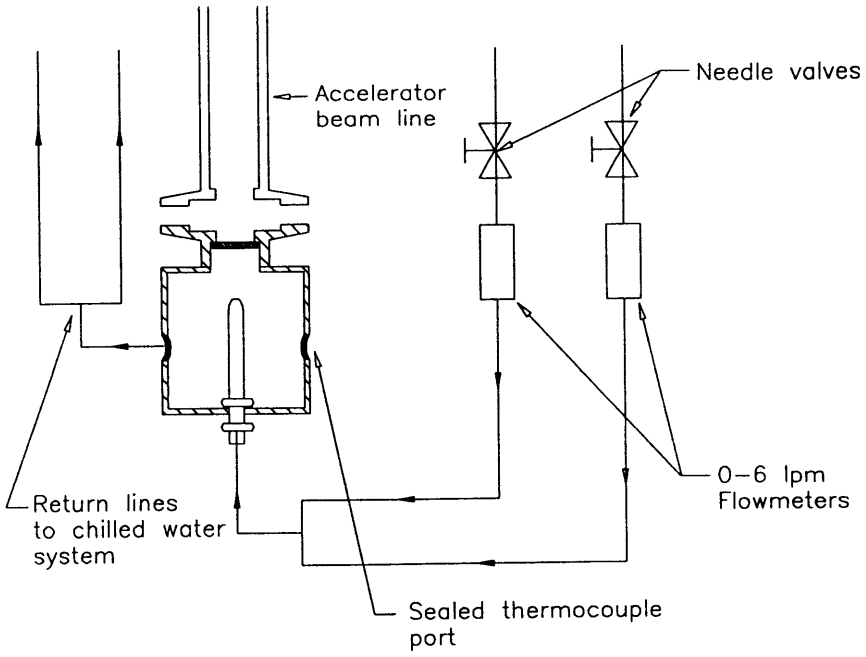

Figure 5.2.1 Illustration of the cooling and flow metering system used in the low power tests.

5.2.2 Evaluation of target power

Determination of the total power placed on target required the measuring of both the current hitting the target and the proton energy. Proton energy was determined by setting the terminal voltage on the accelerator to a known level. The energy of each proton striking the target in MeV, therefore, was simply twice the terminal setting in MV. For example, a terminal setting of 1 MV would result in a proton beam energy of 2 MeV.

Power was adjusted by variation of the target current at a constant beam energy. Current was measured using two UEI DM 410 Digital Multimeters. One of the multimeters was connected to the target housing, while the second was connected to an insulated section of the beam line before the target. By measuring the current striking the target, power was determined by Eq. 5.2.1

$$\text{Power (W)} = \text{Target Current } (\mu\text{A}) \bullet \text{Beam Energy (MeV)} \qquad (5.2.1)$$

5.2.3 Measuring the jet temperature

In order to determine the heat transfer coefficient, the temperature of the cooling jet had to be known. This temperature is referred to as T_∞ , and along with T_s is used to determine the difference in temperature needed to calculate h. In addition to the temperature itself, certain properties such as kinematic viscosity, which is used to determine the Reynolds Number, are evaluated at T_∞. If fluid properties such as conductivity or the Prandtl Number are needed, they are evaluated at the film temperature T_f, where:

$$T_f = (T_s + T_\infty) / 2 \qquad (5.2.2)$$

Measurement of the fluid temperature was performed using a Type K (Cu-CO) thermocouple attached to the metal nozzle just prior to the target housing. In order to

ensure that the thermocouple was accurately measuring the jet temperature, it was surrounded by insulation to keep it separated from the air temperature.

5.2.4 Determination of jet velocity

According to Eq. 3.2.1, the heat transfer coefficient will be some function of the Reynolds number of the cooling fluid. Specifically, the Re used will be that of the fluid as it leaves the nozzle. As noted earlier, the flow rate was measured by two rotameters in parallel which could allow volumetric flow rates of up to 6 LPM (6×10^{-3} m^3 / min). Velocity was simply determined by

$$\text{Jet Velocity (V)} = Q / A \qquad (5.2.3)$$

where Q = volumetric flow rate (m^3 / s)

A = nozzle area (m^2)

Once the jet velocity has been determined, Re can be determined using Eq. 3.2.3.

5.2.5 Measuring the surface temperature

Determination of the surface temperature in contact with the cooling fluid was critical for accurate calculation of the heat transfer coefficient. Normally the front side is monitored by thermocouples and the back temperature is simply calculated based on the measured temperature. Since the front side of the target was under vacuum and could possibly be in the path of the beam, it was not feasible to attach thermocouples there. Originally it was

thought that the front surface temperature could be monitored using an optical pyrometer. Difficulty arises when using the pyrometer, however, because it must be specifically calibrated for each temperature range in which it operates.

Because of this limitation, five Type K thermocouples were epoxied along the back side of the target as shown in Figure 5.2.2.

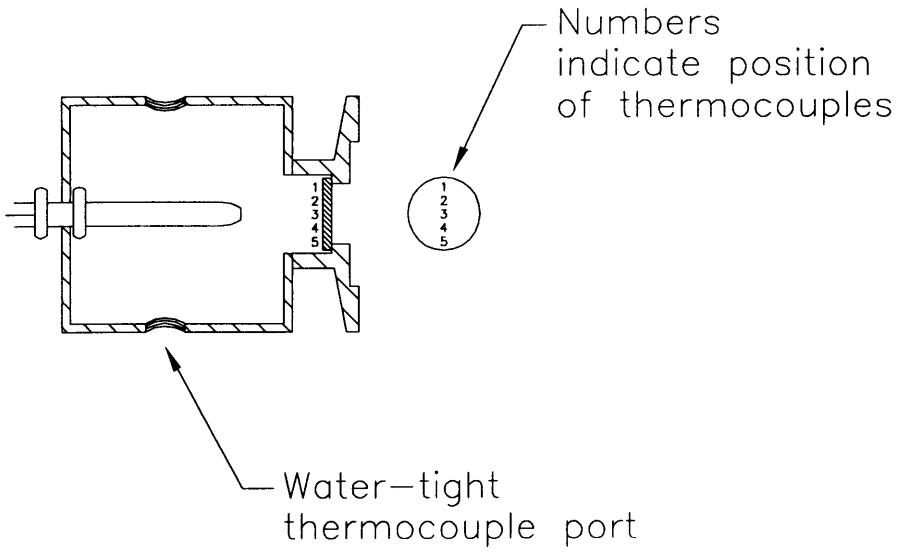

Figure 5.2.2. Position of the five thermocouples used in the low power tests.

When applying these thermocouples it was necessary to keep the wires out of the path of the jet, so as to not disrupt the flow. It was also desirable to keep the mound of epoxy as small as possible on the target surface. When a jet of high velocity strikes a surface and moves outward, the actual heat transfer region between the surface and the ambient fluid

body can be millimeters or less. Any disturbance in the flow might detrimentally affect the heat transfer and should be avoided.

5.2.6 Finding the area normal to heat flow

According to Eq. 3.1.3, the heat flux is dependent on the area of the target normal to the heat flow. Ideally, the power on target would be uniform, and (A) would simply be the area of the target. When using the accelerator to place a beam on target, however, the beam spot size varies considerably with energy and current. Experiments conducted by R.E. Klinkowstein, Haijun Song, and the author [18] indicate that the beam spot can vary from a diameter of 3 mm to a large defocused beam covering more than the entire target area. Control of the beam size was performed by combining the effects of a quadrupole doublet and an X-Y steering magnet. By combining the focusing effects of the quadrupole with the steering magnet, the optical elements were adjusted until it was clear that the entire beam was hitting the target area. Using the data from the beam size experiment, it was determined that the beam used in this experiment covered approximately 1/2 the target area. This area was calculated to be 7.75×10^{-4} m^2.

5.2.7 Calculating h

Once q, A, T_s, and T_∞, had been determined, h could be calculated using 3.1.3. It is important to note that this value is a local value of h based on the postition of the

thermocouple and may or may not be applicable over the entire surface. Discussion as to the variation of the h value was mentioned in Chapter 4 and will be extended in Chapter 7.

5.3 Low Power Test Procedures

Experiments were conducted on the accelerator using two different sized nozzles. The first was a copper nozzle with a diameter of 3.81×10^{-3} m. The second was a stainless steel nozzle of diameter of 2.21×10^{-2} m. In each case, the nozzles were externally marked in increments of Z/D so that various nozzle to target spacings could be examined.

To begin the experiment, the terminal voltage was set at 0.750 MV so that the beam energy was 1.5 MeV. The accelerator was then adjusted so that approximately 100 μA were on target. This setting could be repeated throughout the test with no variation in the terminal, and only deviations of around 1 μA. Starting at a Z/D spacing of 0.5, temperatures from the five thermocouples and the jet temperature were recorded for flow rates from 0.2 LPM up to a maximum of 4 LPM with the smallest nozzle. This was repeated for various settings up to a Z/D of 10.

Tests on the large diameter nozzle were conducted following a similar procedure again at the 150 W level. Measurements were made beginning at a Z/D of 0.25 over a flow rate range from 0.2 to 6 LPM. The maximum Z/D spacing was 2.5. Photographs of the system used in this experiment are shown below in Figure 5.3.1.

In order to increase power levels to the kilowatt level and above, it was necessary to alter the target material and employ a 48 kW power supply. These tests are described in the following section, while the results are presented in Chapter 6.

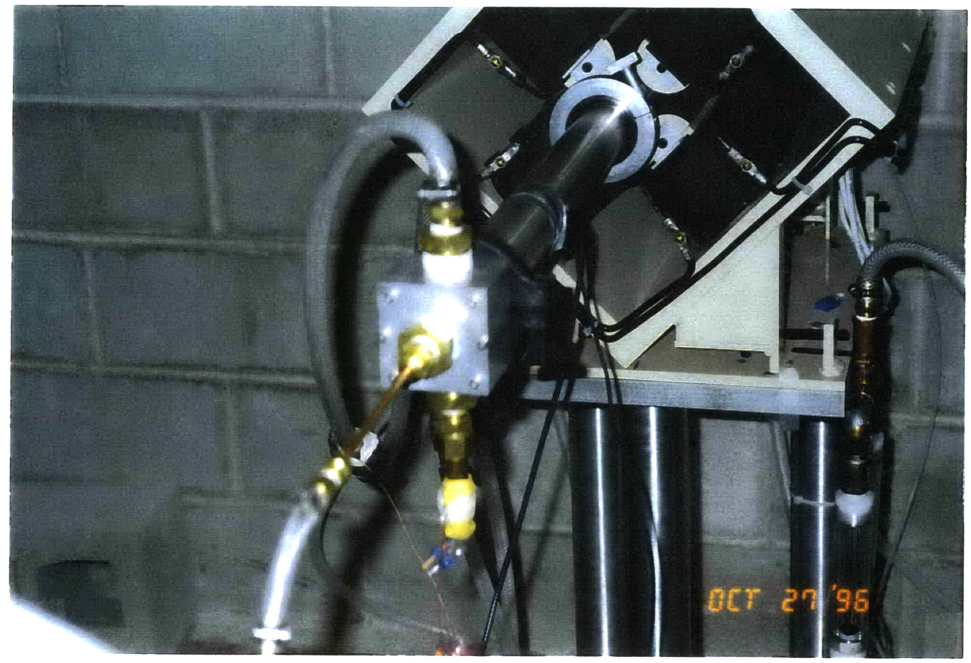

Figure 5.3.1 Photographs of the low power test assembly and cooling system.

5.4 High Power Heat Transfer Experiments

The second major group of experiments were carried out off the accelerator in order to investigate the heat transfer capabilities of the target under high flow rate and high heat load conditions. Using the same target housing from the low power tests, the target itself had to be modified so that it could be heated resistively. This required that the 0.1" thick aluminum target from the previous tests be replaced by a very thin stainless steel target. The cooling and temperature measurements were also adjusted to accommodate the extremely high flow rates used in the experiments.

5.4.1 Configuring the cooling system

The entire cooling system had to be redesigned for the high power tests. Figure 5.4.1 illustrates the setup used in these experiments. Most noticeably, a TEEL 15 HP centrifugal pump served as the source of the cooling flow. In order to keep the suction of the pump flooded, a 90 gallon polyethylene reservoir was positioned above the pump inlet. This large reservoir was needed because as opposed to the low power test, there would be no external cooling source for the water. The experiment relied on the large thermal mass of the water to absorb the power being dissipated from the target.

Immediately following the outlet of the pump, the flow was split into two parrallel sections of 2" ID PVC pipe. On each branch, a ball valve and return line allowed for up to 100% of the flow to be siphoned directly to the reservoir. This enabled the flow to be

adjusted from very low flow rates to extremely high rates without completely blocking the outlet of the pump.

Each branch contained a high capacity in-line flow meter which was used to determine the flow rate. One branch contained an Omega model FL-7325 BR meter with a range of 0-25 GPM and an accuracy of ± 4%. This meter was used as the fine adjust since it indicated flow rate in increments of 1 GPM. The other branch contained a large FL-8313 meter which could handle 10-135 GPM with an accuracy of ± 4%.

Immediately following the flow meters, the lines were joined and connected to a single nozzle on the back of the target housing. Coolant striking the target was vented through two 1" openings on the sides of the housing, and was carried back to the reservoir in parallel flow. Both return lines were constructed so that equal amounts of flow were carried back to the reservoir. This kept the flow at the target uniform in all directions.

5.4.2 Evaluating target power

In order to heat the target, a large DC power supply capable of providing 2200 A at 22 V was used to resistively heat the target. In order to achieve the maximum voltage drop across the target, the 0.1" aluminum target was replaced with a thin stainless steel target. The resistivity of aluminum is about 25 times less than stainless, so it was calculated that a 0.010" thick stainless steel target was needed. This thickness was also needed to support

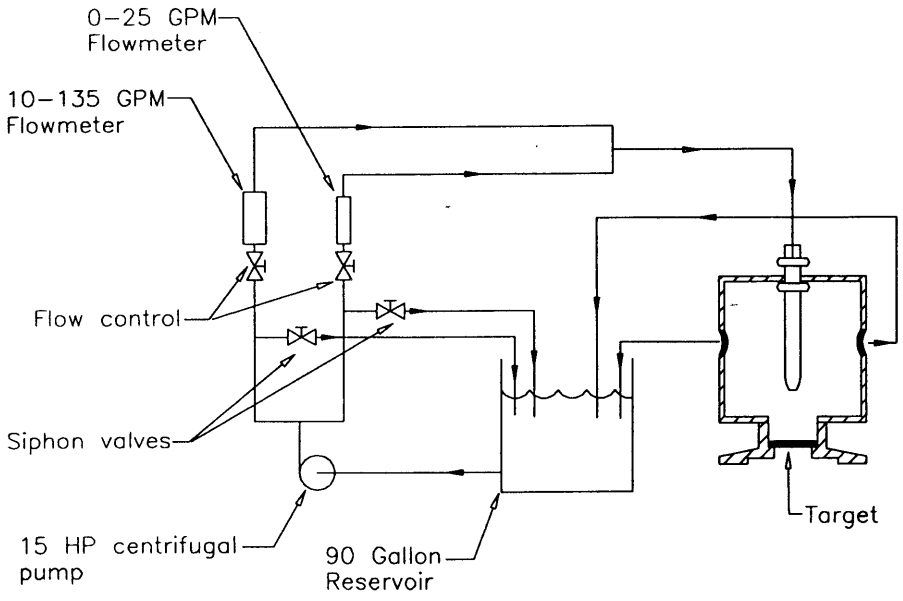

Figure 5.4.1 Cooling system for the high power tests.

the force of a high velocity jet of water. Two targets were constructed with slightly varying thicknesses of steel. One was constructed from 10 mil 302 stainless, while the other was made from 16 mil 304 stainless. Each target had a 1.95" diameter, with an 8" length of 1/4" copper rod brazed to the middle of the target.

In order to pass current through the target, two 15 foot lengths of 4/0 welding cable were connected to the positive terminal of the power supply. These cables were then connected to a single lug which was soldered to the end of the copper rod attached to the target. The target itself was held in place by an insulating KF-50 clamp which compressed the the target onto the aluminum target housing. This clamp not only

provided the electrical connection from the target to the housing, but it also served to make the target water-tight by compressing an O-ring on the back side of the target. A second set of 4/0 welding cables were attached to the back of the target housing and connected to the negative terminal of the power supply. The complete electrical assembly is pictured in Figure 5.4.2.

During the experiments, power was monitored by controlling the current and voltage drop across the target. The current was read directly from a meter on the power supply, while the voltage drop was measured by a Fluke multimeter connected in parallel to the target. Total power was calculated simply by multiplying the current and voltage. It is important to note, however, that the power distribution within the target was not uniform across the entire body of the target. Heat flux is actually peaked at the edge of the copper rod and falls off with a $1 / R^2$ dependence as it moves outward from the center of the target. This distribution can cause the local heat flux to be factors of 10 higher than the average total.

5.4.3 Measuring the jet temperature

As in the previous experiment, the jet temperature was monitored by an insulated Type K thermocouple attached to the jet nozzle just prior to the target housing. For this experiment the monitoring of the jet temperature was more critical because the reservoir tended to heat up due to the work done by the pump and the heat removed from the target. Whereas, the chilled water system in the previous experiment kept the water at a

steady temperature, the reservoir in the high power tests tended to heat up at the rate of about 0.1 degree per minute.

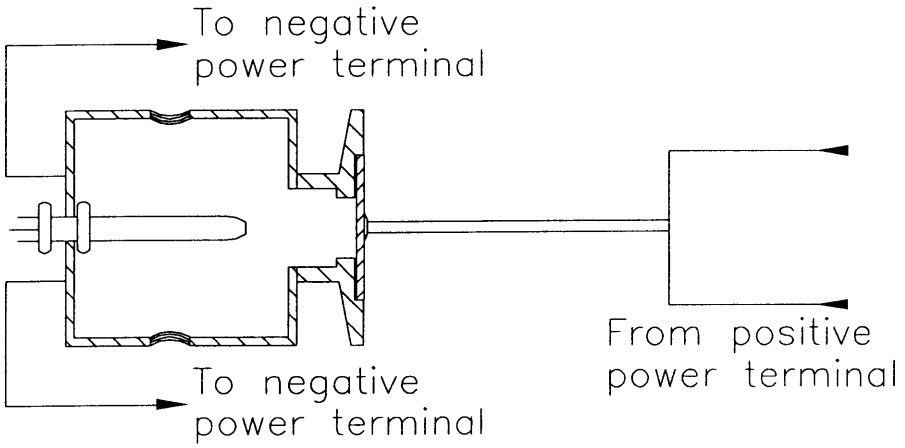

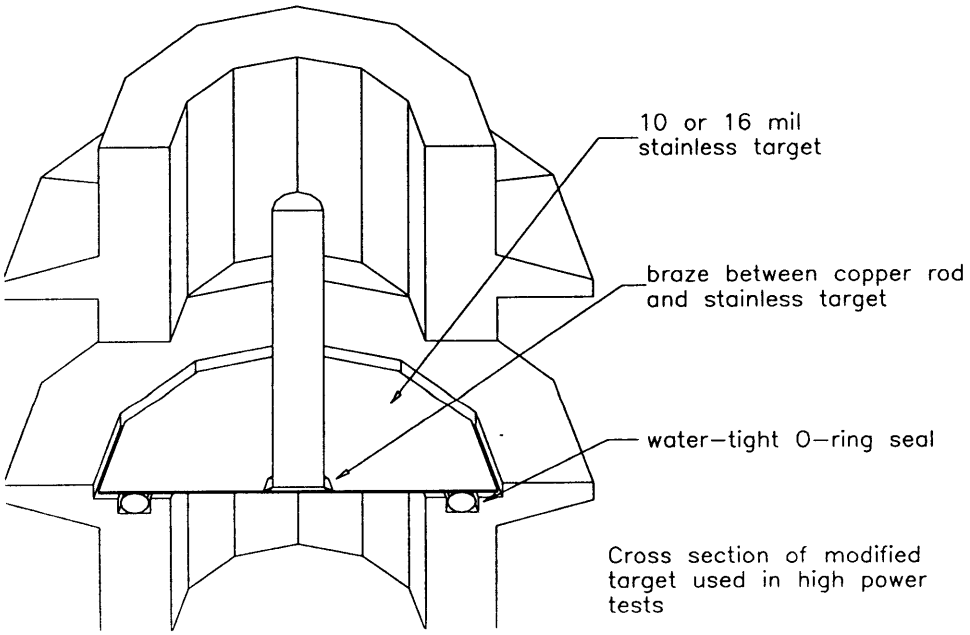

Figure 5.4.2 Diagram of the electrical assembly and target housing.

5.4.4 Determination of jet velocity

Control of the cooling flow was carried out by a set of four 1.25" ball valves, as shown in Fig. 5.4.1. By adjusting the amount of flow that was siphoned directly back into the reservoir, the valves just prior to the flow meters could be used to set the exact flow rate to the target. Once the flow rate was known, the jet velocity was calculated by dividing the flow rate by the area of the nozzle. This velocity could then be used to determine the jet Reynolds number.

5.4.5 Measuring the surface temperature

For the high power tests, it was not possible to affix thermocouples directly to the back of the target because of the high water velocities. In order to determine the temperature of the target in contact with the water, a Type-K thermocouple was epoxied to the front of the target. The radial position of the thermocouple during the various trials was moved and measured in order to investigate the variation in power distribution due to the $1 / R^2$ effect. In order to calculate the back surface temperature of the water, the approximation was made that the front side of the target was insulated. This is in fact a good approximation when the thermal resistances of the jet impingement on the back of the target is compared to the thermal resistance of natural convection and radiation on the front side. With this approximation, the T_s of the back of the target can be calculated by Equation 5.4.1 from [9].

$$T_s = T_0 - \frac{\dot{q}t^2}{2k} \tag{5.4.1}$$

where T_0 : measured temperature on front of target

$\dot{q}$: power per unit volume (W / m^3)

t: thickness of the target (m)

5.4.6 Finding the area normal to heat flow and calculations of h

Determination of the area in the target normal to heat flow, depends strongly on the 1 / R^2 distribution of power. To first order, the area could simply be considered to be the entire area of the target through which is heat generated and flows toward the water. This will give an order of magnitude approximation, but must be adjusted for the power distribution. A more precise determination of the normal area to heat flow can be derived from the definition of power in an electrical circuit.

In the target, current flows from the copper rod outward in the stainless steel until it reaches the aluminum housing. The power generated in a thin annulus of thickness, dr, can be expressed by

$$dP(r) = \frac{I^2 \rho dr}{2\pi rt} \tag{5.4.2}$$

Dividing by a differential area of each annulus, 2πrdr, gives the expression for the heat flux, as a function of r.

$$q''(r) = \frac{I^2}{4\pi^2 t}\frac{1}{r^2} \tag{5.4.3}$$

This equation was used along with Eq. 3.1.3 to calculate h, since the position of the thermocouple (r) was known. Although the average heat flux found by dividing total power by heat generation area may be on the order of several hundred W/cm^2, the local heat flux near the copper rod could be as much as an order of magnitude higher. Because the thermal resistance in the radial direction is significantly more (>400 times) than in the axial direction, there was a negligible effect of the heat flowing away from the copper rod radially out through the target.

5.5 Procedures for the High Power Tests

Experiments using the 48.4 kW power supply investigated the effective cooling rates of a large range of flow values and associated flow velocities with powers up to 6.25 kW over the entire target. Data consisted of measuring the current and voltage drop across the target, as well as the target temperature, jet temperature, and flow rate.

The first set of experiments were conducted on the 10 mil 302 stainless target because it allowed for a greater voltage drop and a higher associated power. Beginning with the 22 mm diameter target at a Z/D spacing of 1, the flow rate was set initially at 10 GPM. The power was set at 157.5 W and the temperatures were measured. Subsequently, the flow rate was increased typically in 5 GPM increments up to 50 GPM.

At each flow rate the power was varied up to around 3 kW. At the highest flow rates, the power was taken to 6.25 kW.

After data was collected at a Z/D of 1, the nozzle was moved back to a Z/D of 2. The preceding steps were repeated, but the target failed at a power level of 4.095 kW and a flow rate of 20 GPM. Reasons for the failure will be discussed later. In order to complete the tests, the 16 mil 304 stainless target was used for the remainder of the experiments. Continuing at a Z/D of 2, the flow was increased to 120 GPM.

The final set of experiments were carried out with the 17 mm diameter nozzle. At a Z/D of 1, the flow was increased from 20 to 70 GPM at a constant power of around 730 W. After the nozzle was moved back to a Z/D of 2, the flow was increased incrementally up to the maximum available flow rate of 87 GPM. Power was incremented at each flow setting. Finally the flow was set at 87 GPM and the power was increased by incrementing the current in steps of 250 amps up to a maximum power of 5.17 kW. Photographs of the high power test assembly are shown below.

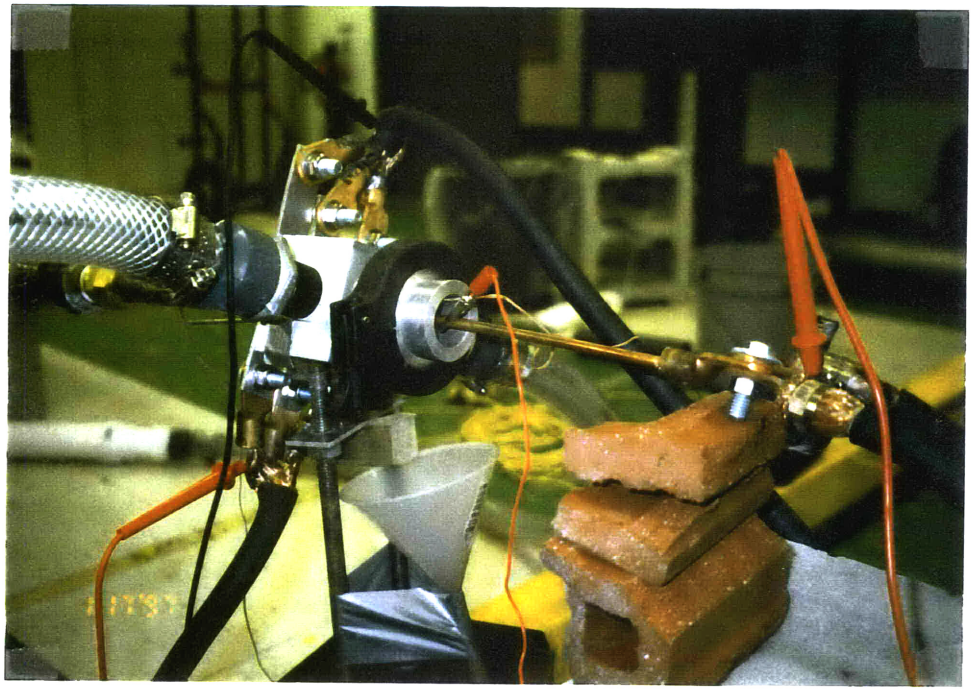

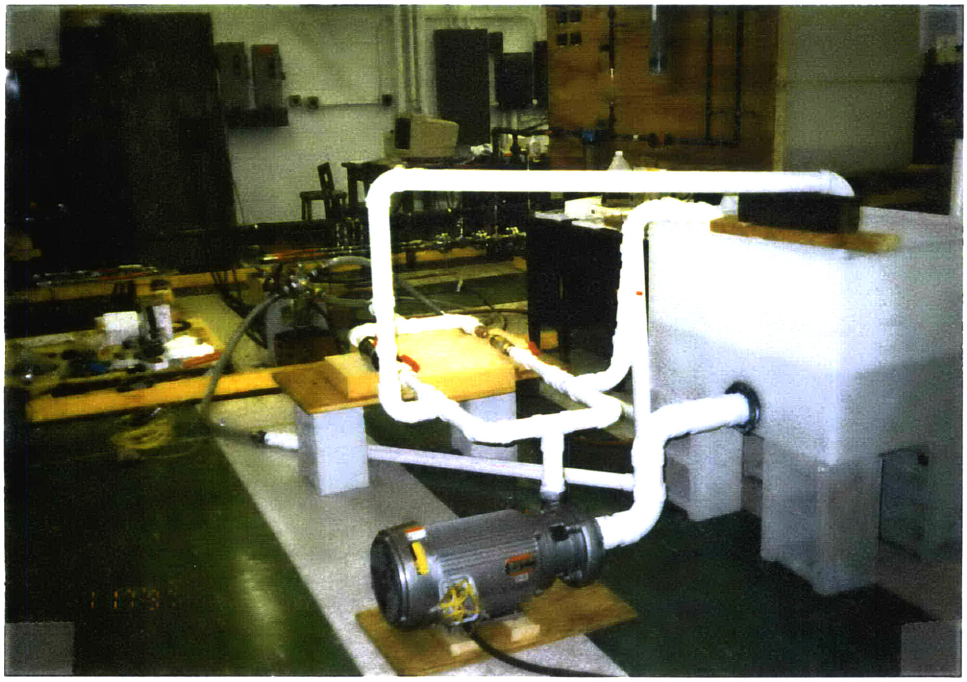

Figure 5.5.1 Photographs of the high power target test assembly.

Chapter 6

EXPERIMENTAL RESULTS

6.1 Explanation of the Data

The following chapter presents the data collected from the two heat transfer experiments conducted both on the accelerator and off the beam line using the 48 kW power supply. The first sections present the raw data from both experiments, while the subsequent sections contain graphs of various cooling characteristics such as h vs. Re and h vs. Z/D.

6.2 Low Power Test Data

Contained in the following tables are the results of the low-power tests of protons on aluminum conducted with the accelerator. Data contained in the tables include the temperature readings from the thermocouples described in Chapter 5 as well as the power levels, flow-rates, and Z/D spacing.

Table 6.2.1 Nozzle Diameter: 0.110" Z/D: 1

Energy	Current	Power	Temp (deg C)							Flow rate
MeV	μA	Watts	1	2	3	4	5	Inlet	Outlet	L / min
1.5	50	75	21.7	24	21.4	20.8	21.1	19.2	20.4	1
1.5	51.5	77.25	21	23	20.9	20.4	21.3	19	20	1
1.5	58.9	88.35	22.1	25	26.4	21.7	21.7	20.5	21.8	1
1.5	60.7	91.05	21.8	23	22.7	22.7	22.5	20.3	21.6	1
1.5	94.6	141.9	23.1	26	23	22.7	24.1	19.6	21.3	1
1.5	98	147	25	30	25.9	23.6	23.4	21.1	22.7	1
1.5	164.1	246.15	27.8	37	28.4	24.5	24.5	21	23.9	1
1.5	187	280.5	23.8	28	24.3	24.5	26.7	19.3	22	1
1.5	222	333	27.2	34	27.4	25.9	26.8	20.4	23.8	1
1.5	228	342	27.2	34	27.7	26.4	27.3	20.4	24	1
1.5	286	429	25.7	33	26.7	26.6	29	19.2	23	1
1.5	315	472.5	25.8	33	27.5	28	31.3	19.1	23.3	1

Table 6.2.2 Nozzle Diameter: 0.870" Z/D: 1

Energy	Current	Power	Temp (deg C)							Flow rate
MeV	μA	Watts	1	2	3	4	5	Inlet	Outlet	L / min
1.5	100.2	150.3	41.1	46	45.6	45.1	35.8	19.6	29.7	0.2
1.5	100.1	150.15	28.7	35	30.7	34.2	36.9	19.9	22.8	0.5
1.5	100.1	150.15	27.1	33	30.2	35.9	38.6	19.8	22.2	0.7
1.5	100.1	150.15	25.9	31	29.2	34.8	37.8	19.9	21.5	1
1.5	100	150	25	30	28.7	34.1	36.8	19.8	21.2	1.3
1.5	100	150	25.1	30	28.4	32.8	36.2	19.8	20.9	1.5
1.5	101	151.5	24.9	30	28.4	32.7	35	19.9	21	1.7
1.5	100.1	150.15	24.6	30	28.2	32	34.7	20	20.9	2
1.5	100	150	24.2	29	27.6	31.6	33.2	19.9	20.6	2.5
1.5	99.7	149.55	24	28	27.4	31.3	32.6	20	20.6	3
1.5	100.1	150.15	23.8	28	27.2	31.2	32.2	20	20.6	3.5
1.5	100	150	23.4	28	27	30.6	31.1	20.1	20.6	4

Table 6.2.3 Nozzle Diameter: 0.870" Z/D: 0.5

Energy	Current	Power	Temp (deg C)							Flow rate	Z / D
MeV	μ A	Watts	1	2	3	4	5	Inlet	Outlet	L / min	
1.5	100.4	150.6	26.7	32	29.9	34	36.3	20.3	21.9	1	0.5
1.5	100.4	150.6	25.1	30	28.5	31.7	33	20.3	21.2	2	0.5
1.5	100.2	150.3	24.5	29	28	30.9	32.2	20.4	21.2	3	0.5
1.5	99.8	149.7	23.9	29	27.6	30.4	30.4	20.4	20.9	4	0.5

Table 6.2.4 Nozzle Diameter: 0.870" Z/D: 0.25-2.5

Energy	Current	Power	Temp (deg C)							Flow rate	Z / D
MeV	μ A	Watts	1	2	3	4	5	Inlet	Outlet	L / min	
1.5	100.8	151.2	24.1	28	26.8	37.1	31.4	18.6	19.8	1	0.25
1.5	101.4	152.1	24.5	29	27.2	37.3	31.6	18.7	20	1	0.5
1.5	101.3	151.95	24.3	28	26.9	37.9	32.9	18.6	19.9	1	0.75
1.5	101.7	152.55	23.8	28	26.9	37.2	33.4	18.6	19.9	1	1
1.5	100.8	151.2	23.2	28	27.5	37.8	34.2	18.6	20	1	1.5
1.5	100.5	150.75	23.2	28	28.6	40.8	34.1	18.7	20	1	2
1.5	100.5	150.75	24.1	30	33.1	44.9	34.1	18.7	20	1	2.5
1.5	100.7	151.05	22.8	26	25.4	32.5	27.1	18.8	19.3	3	0.25
1.5	101.1	151.65	22.3	26	25.5	33.1	27.4	18.5	19.1	3	0.5
1.5	100.6	150.9	22.5	26	25.5	33.2	29.3	18.8	19.3	3	0.75
1.5	100.7	151.05	22.7	26	25.4	33.2	29.7	18.8	19.3	3	1
1.5	100.4	150.6	21.6	26	25.8	34	27.7	18.7	19.3	3	1.5
1.5	100.3	150.45	21.3	26	26.9	35.5	28.4	18.9	19.4	3	2
1.5	100.3	150.45	21.5	26	27	36.5	29.1	18.9	19.4	3	2.5
1.5	100	150	19.9	23	24.1	28.9	24	17.8	18.2	6	0.25
1.5	100	150	20.2	24	24.2	29.9	24.8	17.8	18.1	6	0.5
1.5	100	150	20.9	24	24.1	29.9	26.6	17.7	18.2	6	0.75
1.5	100	150	21.3	24	24.5	30.5	25.9	18.1	18.5	6	1
1.5	100	150	20.9	25	25	31	25.4	18.7	19.1	6	1.5
1.5	100.5	150.75	20.5	25	25.4	32.2	26	18.9	19.2	6	2
1.5	100.7	151.05	20.5	25	25.8	32.3	26	18.8	19.2	6	2.5

Table 6.2.5 Nozzle Diameter: 0.150" Z/D: 1-10

Energy	Current	Power	Temp (deg C)							Flow rate	Z / D
MeV	μ A	Watts	1	2	3	4	5	Inlet	Outlet	L / min	
1.5	100	150	20.5	23	22.9	26.6	23.9	19	19.8	1	1
1.5	100.2	150.3	20	22	22.2	24.5	22.3	19	19.7	2	1
1.5	100.7	151.05	19.5	21	21.6	23.5	21.5	18.9	19.4	3	1
1.5	100.3	150.45	19.5	21	21.5	23	21.3	18.9	19.3	4	1
1.5	100.2	150.3	20.8	23	23.1	26.9	24.2	19.1	20	1	2
1.5	100	150	20	22	22.2	24.6	22.5	19	19.6	2	2
1.5	100.7	151.05	19.4	21	21.6	23.6	21.7	18.8	19.4	3	2
1.5	100.3	150.45	19.6	21	21.6	23.2	21.4	18.9	19.3	4	2
1.5	100.2	150.3	20.9	23	23.3	27.2	24.5	19.1	20.1	1	3
1.5	100.2	150.3	19.8	22	22.3	24.8	22.5	19	19.7	2	3
1.5	100.3	150.45	19.5	21	21.9	24.1	21.9	18.8	19.5	3	3
1.5	100.4	150.6	19.6	21	21.7	23.4	21.4	18.9	19.3	4	3
1.5	100.2	150.3	20.8	23	23.4	27.4	24.6	19.1	20	1	4
1.5	100.4	150.6	20	22	22.4	25.1	22.7	19	19.7	2	4
1.5	100.2	150.3	19.6	21	21.9	24.1	22	18.8	19.5	3	4
1.5	100.1	150.15	19.6	21	21.8	23.5	21.5	18.9	19.3	4	4
1.5	100.7	151.05	20.9	24	23.7	27.9	24.4	18.8	20.3	1	5
1.5	100.7	151.05	20.1	22	22.7	25.2	22.6	18.9	19.8	2	5
1.5	100.7	151.05	20.2	22	22.4	24.4	22	19	19.6	3	5
1.5	100.5	150.75	19.7	21	21.9	23.8	21.6	18.9	19.4	4	5
1.5	101.1	151.65	20.7	23	23.5	28	24.7	18.7	20	1	7
1.5	100.9	151.35	19.8	22	22.5	25.3	22.6	18.6	19.4	2	7
1.5	100.7	151.05	19.4	21	22	24.2	21.7	18.5	19.2	3	7
1.5	100.7	151.05	19.2	21	21.5	23.5	21.2	18.4	19	4	7
1.5	100.2	150.3	20.4	23	23.6	28.5	25	18.2	19.5	1	10
1.5	100.1	150.15	19.7	22	22.8	26.1	22.8	18.3	19.2	2	10
1.5	100.2	150.3	19.6	22	22.5	25	22.2	18.7	19.2	3	10
1.5	100.7	151.05	19.2	21	21.9	24.2	21.6	18.4	19	4	10

Table 6.2.6 Nozzle Diameter: 0.150" Z/D: 1

Energy	Current	Power	Temp (deg C)							Flow rate	Z / D
MeV	μA	Watts	1	2	3	4	5	Inlet	Outlet	L / min	
1.5	100.3	150.45	27	30	25.2	36.7	32.9	17.8	24.6	0.2	1
1.5	100.2	150.3	19.4	22	19.6	27.1	23	15.1	18.2	0.4	1
1.5	100.7	151.05	17.5	20	18.4	24.4	21.4	14.8	17.1	0.6	1
1.5	100.5	150.75	16.9	19	18	23.4	20.4	14.7	16.8	0.8	1
1.5	101.4	152.1	16.4	19	17.7	22.7	19.8	14.6	16.5	1	1

6.3 High-Power Results

The following tables contain the results from the tests conducted with the 48 kW power supply. During the collection of the data, the position of the thermocouple was moved to various locations from the copper rod. Variation in q" based on the $1 / R^2$ power distribution is explained in Chapter 5. The position away from the 0.25" copper rod is listed above each table as the "R" value. Thermocouple position is given in inches from the edge of the copper rod.

Table 6.3.1 Nozzle Diameter: 0.87" Z/D: 2 Target thickness: 10 mil R: 0.3"

Flow Rate	Voltage	Current	Power	Front Temp (T_0)	Jet Temp (T_f)
GPM	V	A	W	°C	°C
10	0.6	500	300	38.9	27.8
10	1.35	1000	1350	74.9	28.3
10	1.71	1250	2137.5	97.9	28.9
20	0.63	500	315	37.3	30
20	1.34	1000	1340	61.2	30.6
20	1.78	1250	2225	91.5	31.3
20	2.1	1500	3150	102.1	32.2
20	2.34	1750	4095	104.7	33.3

Table 6.3.2 Nozzle Diameter: 0.87" Z/D: 1 Target thickness: 10 mil R: 0.3"

Flow Rate	Voltage	Current	Power	Front Temp (T_0)	Jet Temp (T_f)
GPM	V	A	W	°C	°C
9	0.45	350	157.5	26.7	17.2
9	0.84	720	604.8	47	19.3
20	0.88	720	633.6	41.8	20
20	1.17	1000	1170	58.1	22.4
30	1.21	1000	1210	51.9	23.3
35	1.21	1000	1210	52.7	25
35	1.25	1000	1250	52.3	28.7
35	1.44	1000	1440	33.5	13.2
35	2.06	1500	3090	66.6	15.3
37	1.8	1500	2700	77.5	30.3
37	1.95	1500	2925	63.2	18.5
37	2.28	1750	3990	79.2	20.8
40	1.34	1000	1340	51.7	29.8
40	1.85	1500	2775	78.1	31.9
45	1.32	1000	1320	51.8	30.5
50	2.04	1500	3060	66	24.3
50	2.63	2000	5260	84.8	24.8
50	2.84	2200	6248	94.4	26.2

Table 6.3.3 Nozzle Diameter: 0.87" Z/D: 2 Target thickness: 16 mil R: 0.175"

Flow Rate	Voltage	Current	Power	Front Temp (T_0)	Jet Temp (T_f)
GPM	V	A	W	°C	°C
20	0.46	500	230	36	14.6
20	0.73	750	547.5	47.6	15.4
30	0.46	500	230	31.6	16.2
30	0.74	750	555	45.3	17.6
70	0.46	500	230	29.7	19.2
70	0.69	750	517.5	43.6	19.9
70	0.98	1000	980	65.8	20.3
70	1.2	1250	1500	82.6	20.8
80	0.92	1000	920	66.8	26.6
90	0.95	1000	950	62.6	27.1
100	0.47	500	235	27.8	22.8
100	0.73	750	547.5	36.6	23.3
100	0.99	1000	990	60.6	27.6
100	1.02	1000	1020	53.3	24.2
100	1.26	1250	1575	65.8	24.6
117	1	1000	1000	59.9	28.9
120	1.05	1000	1050	58.6	29.5

Table 6.3.4 Nozzle Diameter: 0.67" Z/D: 1 Target thickness: 16 mil R: 0.175"

Flow Rate	Voltage	Current	Power	Front Temp (T_0)	Jet Temp (T_f)
GPM	V	A	W	°C	°C
20	0.93	750	697.5	51.9	20.9
30	0.89	750	667.5	44.8	22.6
35	0.9	750	675	44	23.3
50	0.96	750	720	42.4	24.2
60	0.95	750	712.5	42.1	24.8
70	0.96	750	720	41.6	26
77	0.97	750	727.5	41.3	26.6

Table 6.3.5 Nozzle Diameter: 0.67" Z/D: 2 Target thickness: 16 mil R: 0.175"

Flow Rate	Voltage	Current	Power	Front Temp (T_0)	Jet Temp (T_f)
GPM	V	A	W	°C	°C
80	0.97	750	727.5	39.3	27.2
85	0.97	750	727.5	38.9	27.7
87	0.75	500	375	29.7	28.5
87	0.98	750	735	36	28.6
87	1.24	1000	1240	46.9	29
87	1.4	1250	1750	56	29.1
87	1.6	1500	2400	71	29.4
87	1.78	1750	3115	89.2	29.6

Table 6.3.6 Nozzle Diameter: 0.67" Z/D: 2 Target thickness: 16 mil R: 0.1"

Flow Rate	Voltage	Current	Power	Front Temp (T_0)	Jet Temp (T_f)
GPM	V	A	W	°C	°C
87	0.74	500	370	25.8	15.8
87	0.95	750	712.5	34.2	16
87	1.16	1000	1160	45.4	16.3
87	1.37	1250	1712.5	59.2	16.5
87	1.53	1500	2295	68.3	16.9
87	1.71	1750	2992.5	69.1	17.9
87	1.92	2000	3840	82.5	18.4
87	2.1	2250	4725	103.1	18.8
87	2.2	2350	5170	112.3	20.4

6.4 Heat Transfer Coefficient for Small Re

Taking the raw data listed above the first step was to determine the Reynolds number based on Eq. 3.2.3 and h based on Equation 3.1.3. Although all positions were measured, the center-line heat transfer is of primary concern since the radial variation of h has been characterized previously by Garimella and Rice. It should be noted that the variation with radial position found in these tests match those found in [17]. The one exception was found to be at position 1. At this position, the heat transfer was found to be consistently higher than the rest. This is explained by the fact that in the low power tests, all flow exited the top of the target housing directly above position 1. This concentration of the flow could explain the variation seen in these measurements. A second explanation could also be that the beam position was lower than expected. If this was the case, the heat flux at position 1 would be grossly overestimated leading to an abnormally high h.

The spreadsheet representation of all the calculated coefficients, Reynolds numbers, heat fluences, and heat transfer coefficients can be found in the Appendix. The Figures 6.4.1 and 6.4.2 illustrate the salient results from the measurements with the 0.15" and 0.87" nozzle tests. As mentioned in Chapter 5, the design of the high-power target depended on finding an optimum Z/D spacing for the nozzle. Figures 6.4.3 and 6.4.4 illustrate the results found when the Z/D spacing was varied at a constant Reynolds number.

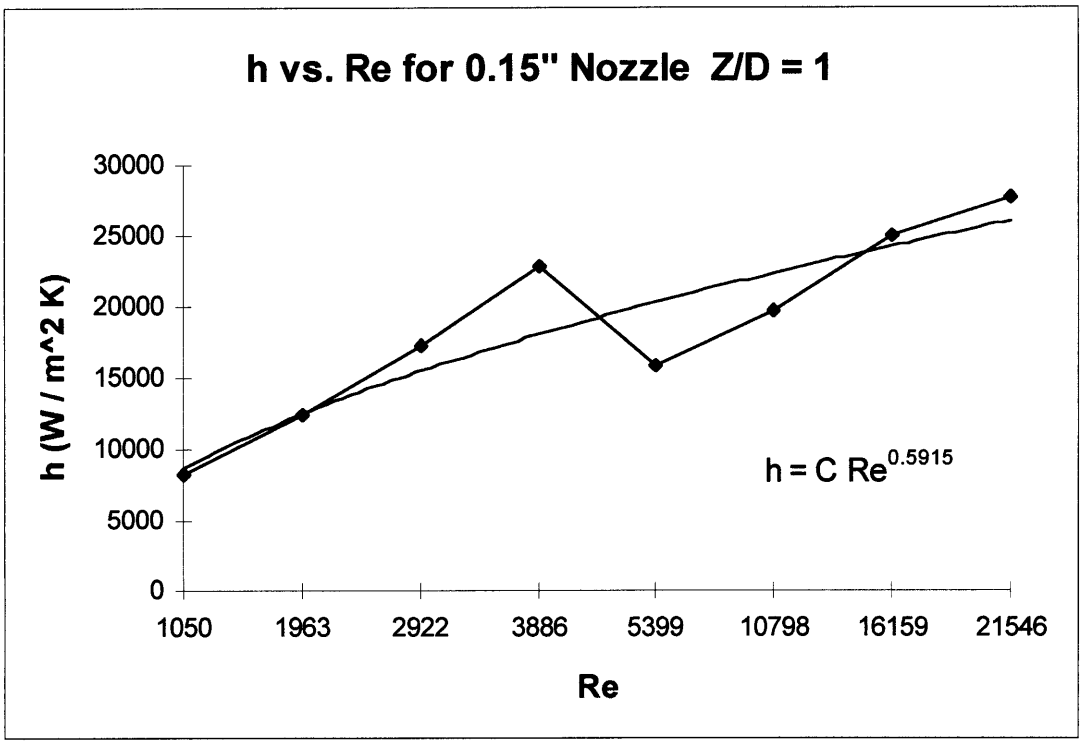

Figure 6.4.1 Variation of h vs. Re for 0.15" nozzle at a Z/D = 1

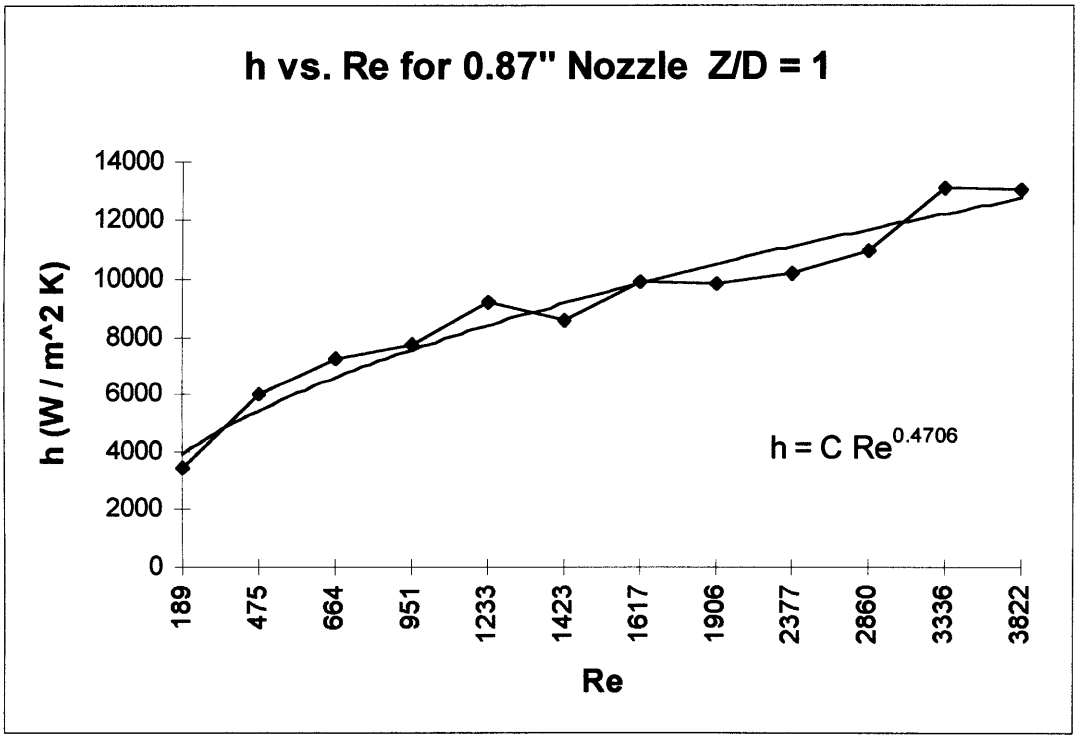

Figure 6.4.2 Variation of h vs. Re for 0.87" nozzle at Z/D = 1

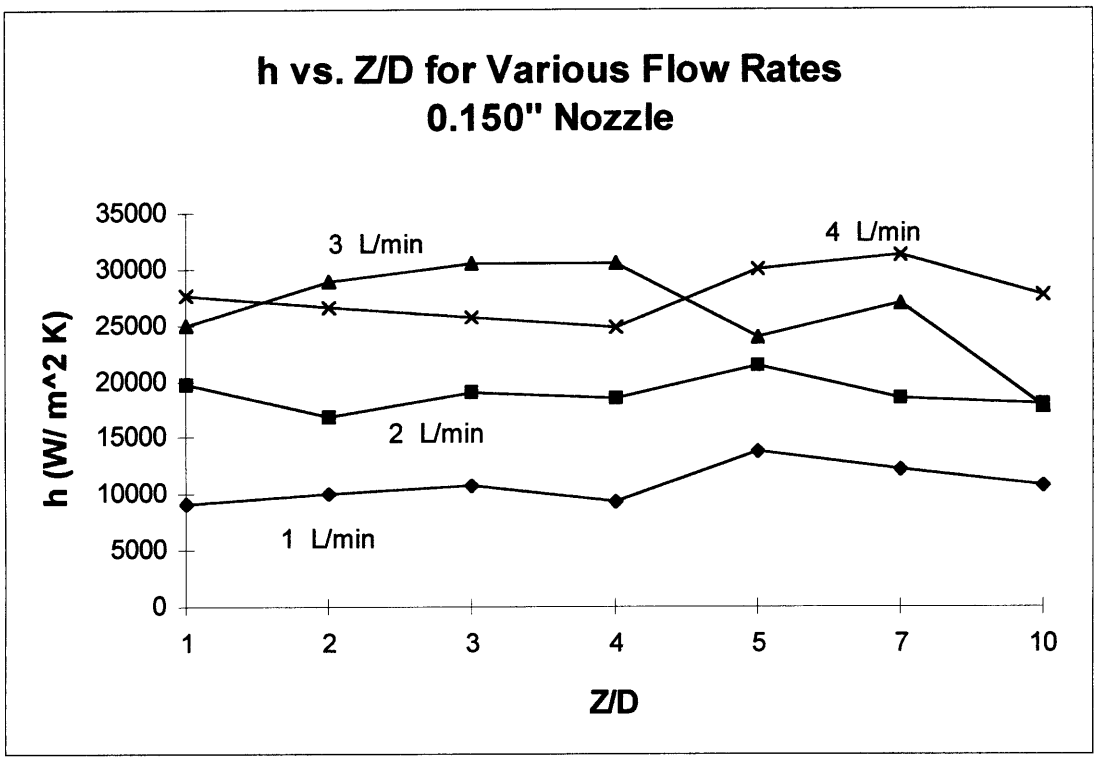

Figure 6.4.3 Variation of heat transfer coefficient with 0.15" nozzle for various Z/D spacing.

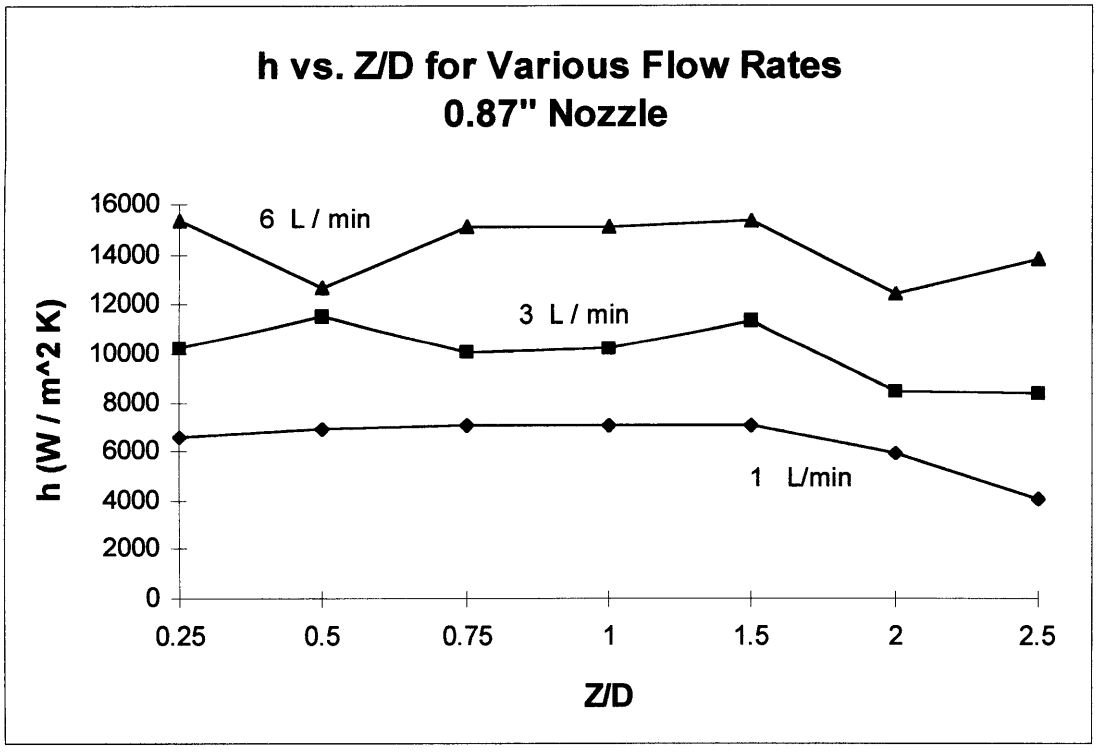

Figure 6.4.4 Variation of heat transfer coefficient with 0.87" nozzle for various Z/D spacing.

6.5 Heat Transfer Coefficient for Large Re

The high power tests were conducted in order to determine the ability of high velocity flows with large Reynolds numbers to remove heat fluences on the order of several kW / cm^2. As was performed with the low power tests, data were entered into a spreadsheet where calculations to determine flow velocity, Re, T_s, and h were carried out. These spreadsheets can be found in the Appendix. Since the variation with Z/D did not seem to affect the heat transfer coefficient especially for higher velocity flows, measurements were made at Z/D spacings of 1 and 2 for both the 0.87" and 0.67" nozzle. For the high power tests, it was important that in looking at the variation of h with Re, the comparisons had to made at similar q" values. As expected, there was a large dependence on q" in the determination of h, which is typical of heat removal systems. As long as CHF is not exceeded, h tends to improve linearly with increases in q". There was clear indication that this was the case in the data collected in this experiment.

The following three figures illustrate the variations at different power levels in the heat transfer coefficient with h. It should be noted that regardless of the spacing or power level, the variation with Reynolds number followed a similar pattern. Again, Z/D spacings did not seem to affect the heat transfer capabilities to any significant extent.

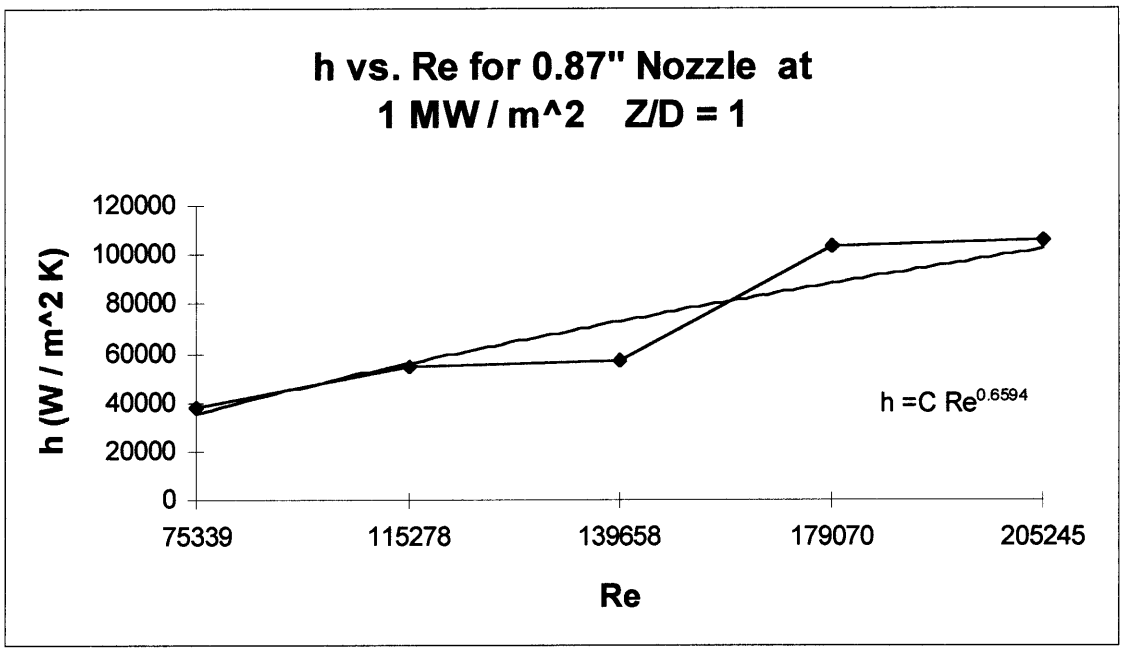

Figure 6.5.1 Heat transfer coefficient vs. Re for 0.87" nozzle at 1 MW / m^2

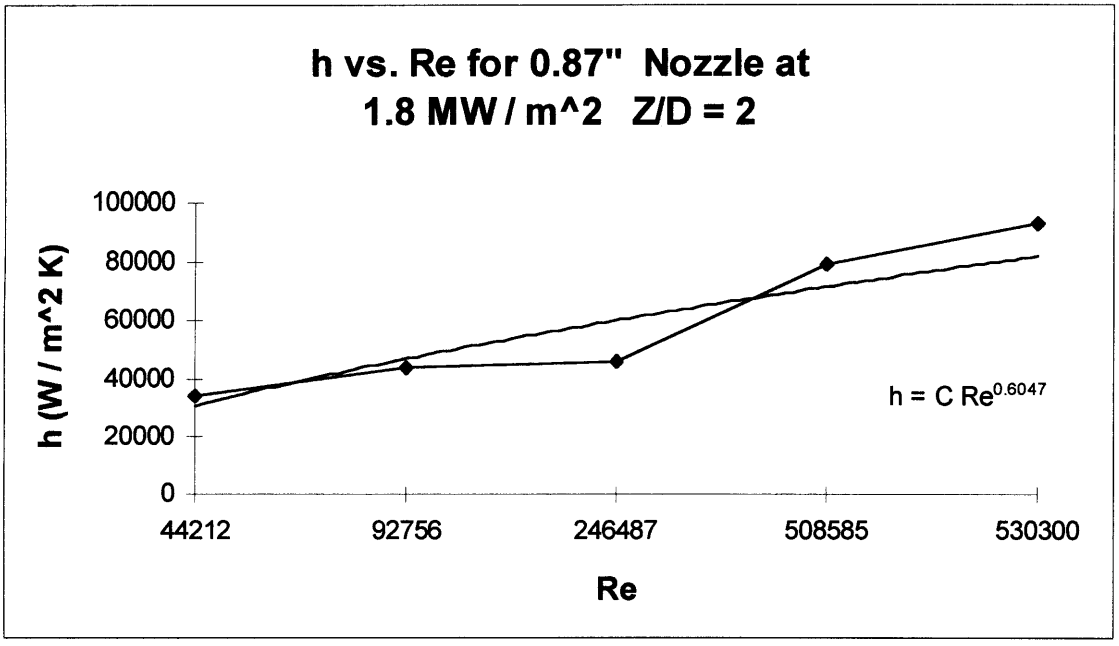

Figure 6.5.2 Heat transfer coefficient vs. Re for 0.87" nozzle at 1.8 MW / m^2

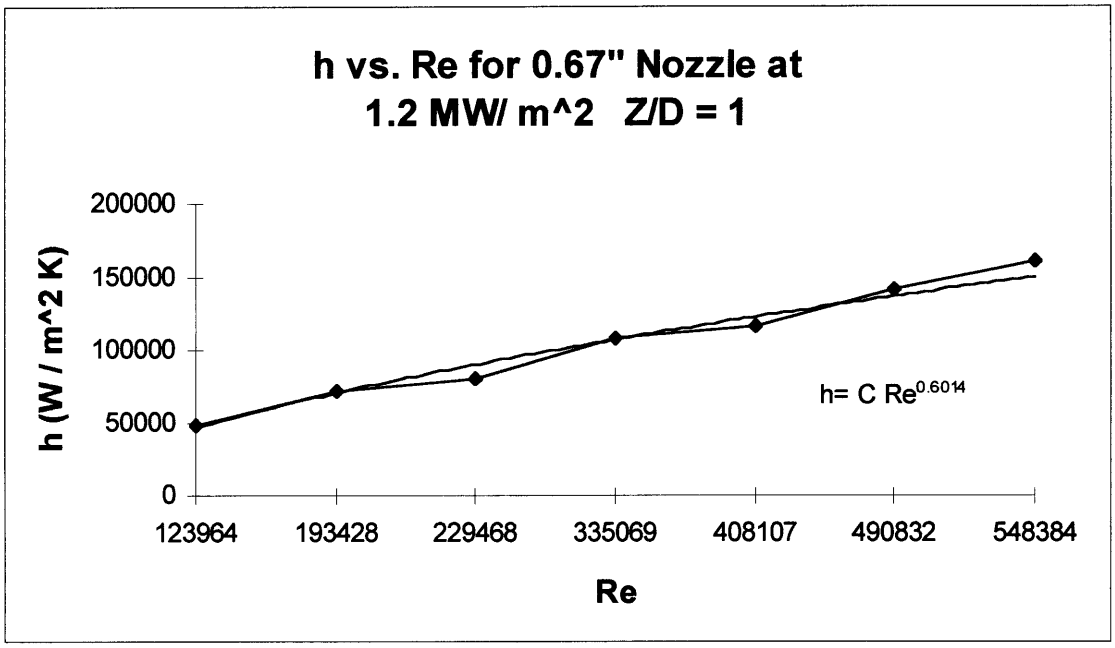

Figure 6.5.3 Heat transfer coefficient vs. Re for 0.67" nozzle at 1.2 MW / m^2

6.6 Burnout in the 10 mil Target

During the testing of the 10 mil target a CHF phenomenon was experienced. At an average target power of 5000 kW and a flow rate of 20 GPM (3.29 m/s) in the 0.87" nozzle, the target suffered a catastrophic burnout. When the heat flux at the copper rod was calculated it was found to be close to 5 kW / cm^2. Eq. 4.6.6 was used to compare this value to the experimental results of Macieka and Skema. The predicted point of failure approximately 2 kW / cm^2. Reasons for this difference will be discussed in the next chapter. A photograph of the burned out target, shown in Figure 6.6.1, indicates that indeed the target failed at the copper rod target interface. When the failure occurred, however, it was not an explosive failure as was first expected. The strength of the target material seemed to prevent a violent destruction from occurring.

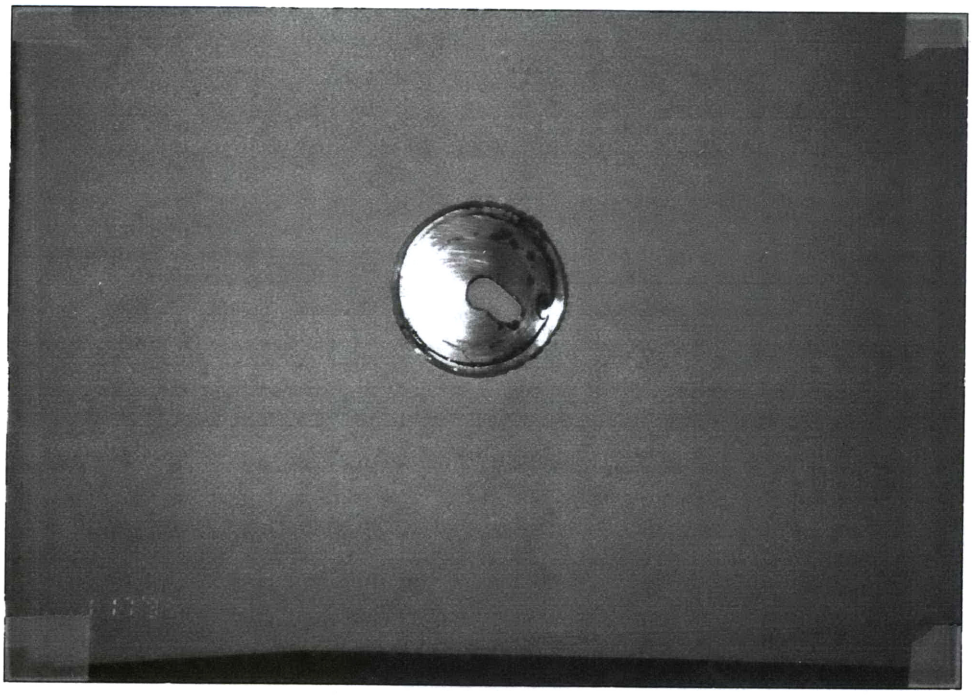

Figure 6.6.1 Ph otograph showing the burnout of the target as a result of DNB.

6.7 Highest Heat Fluences During Test

Due to the limitations of the pump in providing the needed flow, the highest velocity that could be achieved with the pump was 24.13 m/s at a flow rate of 87 GPM in the 0.67" nozzle. At this flow rate, the heat flux at the copper rod was 5.07 kW/cm^2, while the heat transfer coefficient was calculated to be 2.58×10^5 W/m^2. Table 6.7.1 indicates the heat flux at the copper rod, h, and Re for the tests under the highest velocity tests.

Table 6.7.1 Heat transfer coefficient and Re for highest coolant velocities achieved in test

Re	h	q"
	$W / m^2 K$	kW / cm^2
514487.3	162418	1.14
516200	162975	1.68
519661	188183	2.25
528520	280501	2.94
533064	289736	3.77
536755	258342	4.64
552048	258615	5.07

Considering that the variation of both nozzles under high-power tests followed the $Re^{.6}$ trend, the q" that can be handled by the flow at 35 m/s is found to be 6.33 kW / cm^2. Even under conditions tested in this experiment, heat fluences in excess of 5 kW/cm^2, were effectively removed by the coolant.

Chapter 7

CONCLUSIONS

7.1 Completion of Goals

At the outset of this thesis, there were two main goals which were presented as being the foundation and motivation for this work. The first was to characterize the innovative new LABA accelerator. Secondly, and most important, was to investigate the capability of a submerged jet impingement cooling to remove large heat loads with flux densities approaching 6 kW / cm^2.

Characterization of the accelerator as well as primary testing and operation has been completed. Operation has indicated that the efficiency of the accelerator power supply exceeds 90%. Beam current levels and terminal voltage are stable and are easily reproduced. Magnetic suppression of secondary electrons has effectively eliminated all background radiation which would otherwise be produced during accelerator operation.

Testing of the high-power target has demonstrated that heat fluences in excess of 5 kW / cm^2 could be removed by high velocity jet impingement cooling. Extrapolation to slightly higher fluid velocities based on Reynolds number indicates that over 6 kW / cm^2 could be removed by this target.

7.2 Heat Removal Capacity

Construction and testing of a prototype high-power target has been completed. Two working targets have been built with the same dimensions, but different target materials. One target contains a beryllium target while the other substituted an aluminum target for the beryllium. Testing was performed with aluminum so that concomitant production of neutrons could be avoided. Similarities in the conductivity between target materials allow the heat removal relations derived in this study to be applied to the beryllium target with little adjustment. Beryllium, in fact, tends to be a more resilient material than aluminum and is a much better thermal conductor than stainless steel. Its specific heat is the highest of any metal, and its melting point is nearly twice that of aluminum. Regarding its tensile strength, beryllium maintains a tensile strength of over 100 MPa even at temperatures in excess of 600 °C [13].

Under low flow rate conditions, the most effective heat removal was achieved by the 0.15" nozzle and scales as $Re^{0.59}$. The 0.87" nozzle heat transfer scales as $Re^{0.47}$. Z/D spacing was found to be relatively unimportant to the effectiveness of heat removal as long as velocity of the jet was high. When testing the 0.87" nozzle under low flow rate conditions, there was a reduction in h as Z/D was increased. As the Z/D spacing for low flow rates are increased, the geometry of the cooling system approaches the limit of pool boiling. In order to maintain high heat removal, it was imperative to keep the velocity of the jet large. When cooling a target, the Reynolds number should be kept above 2300, which marks the beginning of turbulent flow. For the 0.87" nozzle, a flow rate of 2.5 L/

min marks the onset of turbulence. The heat transfer coefficient for the small nozzle varied only slightly as Z/D was increased.

When the target was tested under high-power, the heat transfer coefficient scaled between the range of $Re^{0.6}$ to $Re^{0.65}$ depending on heat flux levels and nozzle diameter. Tested under the highest coolant velocity of 24.13 m/s, the target was able to effectively handle a maximum heat flux of 5.07 kW/cm^2. Using the scaling of $Re^{0.6014}$ for the 0.67" nozzle, at a fluid velocity of 35 m/s, 6.33 kW/cm^2 could be removed. The improvement in the conductivity of beryllium would most likely increase these numbers. It is therefore reasonable to predict that 50 kW or more could be safely handled by the beryllium target.

According to Maceika and Skema, at a 35.3 m/s the CHF was found to be around 6 kW/cm^2, which agrees with the results found in this experiment. In the target tested during this experiment, in fact, the heat transfer values and CHF values were higher than those found by Maceika and Skema. As mentioned earlier, the q" during the burnout of the 10 mil target was found to be 4.9 kW/cm^2. This burnout occurred at a flow velocity of 3.29 m/s. Using Eq. 4.6.6, the calculated CHF was 2.83 kW/cm^2. The improvement in the CHF level is most likely due to the pressure increase in the target. Soviet experiments found that pressure in the target never rose above 28 psi, whereas pressure in the high-power target was between 60-65 psi. This increase in pressure raises the saturation point of the water resulting in a higher CHF value.

7.3 Liquid Erosion of Target

Although quantifying the rate at which the target is eroded by a high velocity jet is difficult, an empirical relation presented in [19] was used to estimate the erosion rate for a 17 mm jet at 24.13 m/s. Using the relation it was found that it would take 830 hours of constant operation to erode the entire target. This is definitely an area which should be investigated further in future work.

7.4 Z/D Spacing

No conclusive evidence was found to warrant a specific Z/D spacing as being more effective than another. Spacing does become important when flow velocity is low. Spacing should be kept between a Z/D value of 1-5 to allow the potential core to strike the target. Spacing the target farther than 5 Z/D allows for the break down of a well-defined jet into smaller individual droplets. Over time, this droplet effect could increase the erosion rate of the target. A small Z/D spacing also maintains a large dynamic fluid pressure on the back of the target, thereby keeping the saturation point at a high level.

7.5 System Strengths

The cooling system designed and tested during these experiments is an effective means of removing high loads with minimal target machining. Use of a single nozzle instead of cooling channels or fins, allows the system to be altered easily and quickly. Plumbing of the system is readily workable, and could easily be adapted to a clinical environment. One

drawback of the system is that the 15 HP pump needed to achieve such high flow rates, requires a substantial amount of power.

7.6 Future Work

The next step of testing the target would be to put the actual beryllium target on the beam line in order to test it under an actual neutron producing environment. Comparison of temperature measurements made with an optical pyrometer could be used to test the actual target against the results gained from the aluminum prototype. Secondly, the target should be reconfigured so that it could fit into an existing LABA moderator in order to produce an epithermal beam of neutrons. Reconfiguring the target could be done by making the target housing cylindrical with the nozzle concentric to the outer housing.

7.7 Implications for BNCT

This work indicates that a beryllium target can be sufficiently cooled to allow the delivery of 15 RBE-Gy to a tumor at a 6 cm depth using a 2.5 mA proton beam of energy 4 MeV on beryllium for 60 minutes. 15-40 RBE-Gy is deliverable to a tumor up to 4 cm in depth in a time of 40-115 minutes [2].

APPENDIX

Listed in the following tables are the spreadsheets used to make heat transfer coefficient calculations with the data from the experiments. The first set of tables are from the low power experiments, while the second set is from the high power experiments.

10/21/96 rotons on Aluminum0.110" Diameter Nozzle

Energy	Current	Power	Temp (deg C)							Flow rate	Mass flow	Z / D	Viscosity	Reynold's	Calculated heat transfer coefficient by position					m c delta T
MeV	micro A	Watts	1	2	3	4	5	Inlet	Outlet	L / min	kg / sec			Number	1	2	3	4	5	
1.5	0	0	19.4	19		19.3	19.3	19.5	19.5	1	0.016667	1	0.00102	7449.8107	0	0		0	0	0
1.5	0	0	19.4	19		19.4	19.4	19.5	19.5	1	0.016667	1	0.00102	7449.8107	0	0		0	0	0
1.5	0	0	19	19		19	19	19.2	19.2	1	0.016667	1	0.001027	7397.1347	0	0		0	0	0
1	57.6	57.6	18.7	19		18.9	18.6	18.4	18.5	1	0.016667	1	0.001046	7260.2397	14989.25	4996.416		8993.548	22483.87	6.97
1	57.9	57.9	19.1	20		19.3	19.1	18.8	19	1	0.016667	1	0.001036	7328.0479	29978.49	8993.548		17987.1	29978.49	13.94
1.5	95	142.5	20.6	22		21.1	21	19.2	20.3	1	0.016667	1	0.001027	7397.1347	35331.8	18320.19		26033.96	27480.29	76.67
1.5	100	150	20.5	22		21.1	21	19.2	20.2	1	0.016667	1	0.001027	7397.1347	34590.57	17295.29		23667.23	24982.08	69.7
1.5	158	237	21.6	24		20.3	20.6	19.2	20.9	1	0.016667	1	0.001027	7397.1347	31852.15	14989.25		69495.6	54603.69	118.49
1.5	161	241.5	22	24		24	23.3	19.4	21.4	1	0.016667	1	0.001022	7432.1688	34590.57	19551.19		19551.19	23060.38	139.4
1.5	161	241.5	21.9	24		24.8	23.7	19.3	21.6	1	0.016667	1	0.001024	7414.6104	39779.16	22005.49		18804.69	23505.87	160.31
1.44	205	295.2	22.4	25		25.7	24.6	19.3	22	1	0.016667	1	0.001024	7414.6104	39165.45	22075.07		18970.77	22908.09	188.19

10/22/96 rotons on Aluminum0.110" Diameter Nozzle

Energy	Current	Power	Temp (deg C)							Flow rate	Mass flow	Z / D	Viscosity	Reynold's	Calculated heat transfer coefficient by position					m c delta T
MeV	μ A	Watts	1	2	3	4	5	Inlet	Outlet	L / min	kg / sec			Number	1	2	3	4	5	
1.5	50	75	21.7	24	21.4	20.8	21.1	19.2	20.4	1	0.016667	1	0.001027	7397.1347	19354.84	9874.918	21994.13	30241.94	25466.89	75
1.5	51.5	77.25	21	23	20.9	20.4	21.3	19	20	1	0.016667	1	0.001032	7362.4292	22483.87	11530.19	23667.23	32119.82	19551.19	69.7
1.5	58.9	88.35	22.1	25	26.4	21.7	21.7	20.5	21.8	1	0.016667	1	0.000995	7630.9474	36536.29	14258.06	9908.147	48715.05	48715.05	90.61
1.5	60.7	91.05	21.8	23	22.7	22.7	22.5	20.3	21.6	1	0.016667	1	0.001	7594.0188	38972.04	22483.87	24357.53	24357.53	26571.85	90.61
1.5	94.6	141.9	23.1	26	23	22.7	24.1	19.6	21.3	1	0.016667	1	0.001017	7467.5365	21841.47	11241.94	22483.87	24659.73	16987.81	118.49
1.5	98	147	25	30	25.9	23.6	23.4	21.1	22.7	1	0.016667	1	0.000981	7743.9201	18448.3	8269.93	14989.25	28779.35	31281.91	111.52
1.5	164.1	246.2	27.8	37	28.4	24.5	24.5	21	23.9	1	0.016667	1	0.000983	7724.8596	19177.42	8253.573	17622.49	37258.99	37258.99	202.13
1.5	187	280.5	23.8	28	24.3	24.5	26.7	19.3	22	1	0.016667	1	0.001024	7414.6104	26980.65	13796.92	24282.58	23348.64	16407.15	188.19
1.5	222	333	27.2	34	27.4	25.9	26.8	20.4	23.8	1	0.016667	1	0.000998	7612.4383	22483.87	11325.21	21841.47	27798.24	23889.11	236.98
1.5	228	342	27.2	34	27.7	26.4	27.3	20.4	24	1	0.016667	1	0.000998	7612.4383	23806.45	12080.89	22175.87	26980.65	23461.43	250.92
1.5	286	429	25.7	33	26.7	26.6	29	19.2	23	1	0.016667	1	0.001027	7397.1347	26288.83	12752.05	22783.66	23091.54	17436.47	264.86
1.5	315	472.5	25.8	33	27.5	28	31.3	19.1	23.3	1	0.016667	1	0.001029	7379.7411	28188.73	13207.31	22483.87	21220.73	15480.7	292.74

10/23/96 Protons on Aluminu 0.870" Diameter Nozzle

Energy	Current	Power	Temp (deg C)							Flow rate	Mass flow	Z / D	Viscosity	Reynold's	Calculated heat transfer coefficient by position				m c delta T
MeV	micro A	Watts	1	2	3	4	5	Inlet	Outlet	L / min	kg / sec			Number	1	2	3	4	5	
1.5	100.4	150.6	26.7	32	29.9	34	36.3	20.3	21.9	1	0.016667	0.5	0.001	960.1633	11241.94	5995.699	7494.624	5251.707	4496.774	111.52
1.5	100.4	150.6	25.1	30	28.5	31.7	33	20.3	21.2	2	0.033333	0.5	0.001	1920.3266	16862.9	8344.529	9870.968	7100.17	6373.381	125.46
1.5	100.2	150.3	24.5	29	28	30.9	32.2	20.4	21.2	3	0.05	0.5	0.000998	2887.4766	26322.58	12404.89	14200.34	10278.34	9145.981	167.28
1.5	99.8	149.7	23.9	29	27.6	30.4	30.4	20.4	20.9	4	0.066667	0.5	0.000998	3849.9688	25695.85	11103.15	12491.04	8993.548	8993.548	139.4
1.5	100.2	150.3	41.1	46	45.6	45.1	35.8	19.6	29.7	0.2	0.003333	1	0.001017	188.83426	4224.876	3466.979	3493.648	3562.151	5607.089	140.794
1.5	100.1	150.2	28.7	35	30.7	34.2	36.9	19.9	22.8	0.5	0.008333	1	0.00101	475.47965	7409.457	4465.974	6037.336	4559.666	3835.484	101.065
1.5	100.1	150.2	27.1	33	30.2	35.9	38.6	19.8	22.2	0.7	0.011667	1	0.001012	664.08007	10348.74	5856.264	7264.02	4692.286	4018.394	117.096
1.5	100.1	150.2	25.9	31	29.2	34.8	37.8	19.9	21.5	1	0.016667	1	0.00101	950.9593	11991.4	6367.114	7736.386	4828.751	4019.463	111.52
1.5	100	150	25	30	28.7	34.1	36.8	19.8	21.2	1.3	0.021667	1	0.001012	1233.2916	15738.71	7720.876	9195.651	5723.167	4814.194	126.854
1.5	100	150	25.1	30	28.4	32.8	36.2	19.8	20.9	1.5	0.025	1	0.001012	1423.0287	13999.39	7346.215	8627.532	5707.444	4524.194	115.005
1.5	101	151.5	24.9	30	28.4	32.7	35	19.9	21	1.7	0.028333	1	0.00101	1616.6308	16817.94	8580.579	9892.903	6569.506	5568.853	130.339
1.5	100.1	150.2	24.6	30	28.2	32	34.7	20	20.9	2	0.033333	1	0.001007	1906.4874	17596.07	8520.204	9870.968	6745.161	5506.254	125.46
1.5	100	150	24.2	29	27.6	31.6	33.2	19.9	20.6	2.5	0.041667	1	0.00101	2377.3983	18300.83	8942.449	10219.94	6725.944	5916.808	121.975
1.5	99.7	149.6	24	28	27.4	31.3	32.6	20	20.6	3	0.05	1	0.001007	2859.7312	20235.48	9752.04	10938.1	7163.003	6423.963	125.46
1.5	100.1	150.2	23.8	28	27.2	31.2	32.2	20	20.6	3.5	0.058333	1	0.001007	3336.353	24850.59	11804.03	13115.59	8431.452	7772.202	146.37
1.5	100	150	23.4	28	27	30.6	31.1	20.1	20.6	4	0.066667	1	0.001005	3822.1566	27253.18	11530.19	13034.13	8565.284	8175.953	139.4

10/24/97 rotons on Aluminum 0.870" Diameter Nozzle

Energy	Current	Power	Temp (deg C)							Flow rate	Mass flow	Z / D	Viscosity	Reynold's	Calculated heat transfer coefficient by position				m c delta T
MeV	micro A	Watts	1	2	3	4	5	Inlet	Outlet	L / min	kg / sec			Number	1	2	3	4	5	
1.5	100.8	151.2	24.1	28	26.8	37.1	31.4	18.6	19.8	1	0.016667	0.25	0.001041	922.22814	9811.144	5784.872	6580.645	2916.827	4215.726	83.64
1.5	101.4	152.1	24.5	29	27.2	37.3	31.6	18.7	20	1	0.016667	0.5	0.001039	924.37645	10078.98	5904.855	6877.419	3142.907	4531.633	90.61
1.5	101.3	152	24.3	28	26.9	37.9	32.9	18.6	19.9	1	0.016667	0.75	0.001041	922.22814	10255.8	6218.943	7043.14	3028.915	4087.977	90.61
1.5	101.7	152.6	23.8	28	26.9	37.2	33.4	18.6	19.9	1	0.016667	1	0.001041	922.22814	11241.94	6218.943	7043.14	3142.907	3949.869	90.61
1.5	100.8	151.2	23.2	28	27.5	37.8	34.2	18.6	20	1	0.016667	1.5	0.001041	922.22814	13685.83	6842.917	7073.577	3278.898	4035.567	97.58
1.5	100.5	150.8	23.2	28	28.6	40.8	34.1	18.7	20	1	0.016667	2	0.001039	924.37645	12990.68	6354.137	5904.855	2645.161	3795.978	90.61
1.5	100.5	150.8	24.1	30	33.1	44.9	34.1	18.7	20	1	0.016667	2.5	0.001039	924.37645	10825.57	5363.125	4059.588	2231.224	3795.978	90.61
1.5	100.7	151.1	22.8	26	25.4	32.5	27.1	18.8	19.3	3	0.05	0.25	0.001036	2779.6044	16862.9	9239.947	10219.94	4923.475	8126.7	104.55
1.5	101.1	151.7	22.3	26	25.5	33.1	27.4	18.5	19.1	3	0.05	0.5	0.001044	2760.2694	21300.51	10792.26	11563.13	5543.968	9094.599	125.46
1.5	100.6	150.9	22.5	26	25.5	33.2	29.3	18.8	19.3	3	0.05	0.75	0.001036	2779.6044	18230.17	9368.28	10067.4	4684.14	6423.963	104.55
1.5	100.7	151.1	22.7	26	25.4	33.2	29.7	18.8	19.3	3	0.05	1	0.001036	2779.6044	17295.29	9500.227	10219.94	4684.14	6188.221	104.55
1.5	100.4	150.6	21.6	26	25.8	34	27.7	18.7	19.3	3	0.05	1.5	0.001039	2773.1294	27911.01	11903.23	11400.27	5290.323	8993.548	125.46
1.5	100.3	150.5	21.3	26	26.9	35.5	28.4	18.9	19.4	3	0.05	2	0.001034	2786.1097	28104.84	9919.355	8431.452	4063.35	7100.17	104.55
1.5	100.3	150.5	21.5	26	27	36.5	29.1	18.9	19.4	3	0.05	2.5	0.001034	2786.1097	25942.93	9500.227	8327.36	3832.478	6612.903	104.55
1.5	100	150	19.9	23	24.1	28.9	24	17.8	18.2	6	0.1	0.25	0.001061	5432.3676	46082.95	18259.28	15360.98	8718.396	15608.74	150
1.5	100	150	20.2	24	24.2	29.9	24.8	17.8	18.1	6	0.1	0.5	0.001061	5432.3676	33725.81	13955.51	12647.18	6689.416	11563.13	125.46
1.5	100	150	20.9	24	24.1	29.9	26.6	17.7	18.2	6	0.1	0.75	0.001063	5420.0011	30241.94	15608.74	15120.97	7932.311	10873.5	150
1.5	100	150	21.3	24	24.5	30.5	25.9	18.1	18.5	6	0.1	1	0.001053	5469.808	30241.94	15360.98	15120.97	7804.37	12406.95	150
1.5	100	150	20.9	25	25	31	25.4	18.7	19.1	6	0.1	1.5	0.001039	5546.2587	43988.27	16685.21	15360.98	7867.821	14443.91	150
1.5	100.5	150.8	20.5	25	25.4	32.2	26	18.9	19.2	6	0.1	2	0.001034	5572.2194	50588.71	14453.92	12452.61	6085.86	11400.27	125.46
1.5	100.7	151.1	20.5	25	25.8	32.3	26	18.8	19.2	6	0.1	2.5	0.001036	5559.2088	56926	16685.21	13824.88	7168.459	13440.86	150

10/24/96 rotons on Aluminum 0.150" Diameter Nozzle

Energy	Current	Power	Temp (deg C)							Flow rate	Mass flow	Z / D	Viscosity	Reynold's	Calculated heat transfer coefficient by position					m c delta T
MeV	micro A	Watts	1	2	3	4	5	Inlet	Outlet	L / min	kg / sec			Number	1	2	3	4	5	
1.5	100	150	20.5	23	22.9	26.6	23.9	19	19.8	1	0.016667	1	0.001032	5399.1148	23982.8	8774.194	9224.152	4733.447	7341.672	55.76
1.5	100.2	150.3	20	22	22.2	24.5	22.3	19	19.7	2	0.033333	1	0.001032	10798.23	62954.84	21708.57	19673.39	11446.33	19077.22	97.58
1.5	100.7	151.1	19.5	21	21.6	23.5	21.5	18.9	19.4	3	0.05	1	0.001034	16159.436	112419.4	30659.82	24982.08	14663.39	25942.93	104.55
1.5	100.3	150.5	19.5	21	21.5	23	21.3	18.9	19.3	4	0.066667	1	0.001034	21545.915	119914	34261.14	27672.46	17548.39	29978.49	111.52
1.5	100.2	150.3	20.8	23	23.1	26.9	24.2	19.1	20	1	0.016667	2	0.001029	5411.8102	23806.45	9635.945	10117.74	5188.586	7935.484	62.73
1.5	100	150	20	22	22.2	24.6	22.5	19	19.6	2	0.033333	2	0.001032	10798.23	53961.29	18607.34	16862.9	9635.945	15417.51	83.64
1.5	100.7	151.1	19.4	21	21.6	23.6	21.7	18.8	19.4	3	0.05	2	0.001036	16121.705	134903.2	35192.15	28907.83	16862.9	27911.01	125.46
1.5	100.3	150.5	19.6	21	21.6	23.2	21.4	18.9	19.3	4	0.066667	2	0.001034	21545.915	102783.4	34261.14	26647.55	16732.18	28779.35	111.52
1.5	100.2	150.3	20.9	23	23.3	27.2	24.5	19.1	20.1	1	0.016667	3	0.001029	5411.8102	24982.08	10457.61	10706.61	5551.573	8327.36	69.7
1.5	100.2	150.3	19.8	22	22.3	24.8	22.5	19	19.7	2	0.033333	3	0.001032	10798.23	78693.55	21708.57	19077.22	10854.28	17987.1	97.58
1.5	100.3	150.5	19.5	21	21.9	24.1	21.9	18.8	19.5	3	0.05	3	0.001036	16121.705	134903.2	39346.77	30462.02	17817.41	30462.02	146.37
1.5	100.4	150.6	19.6	21	21.7	23.4	21.4	18.9	19.3	4	0.066667	3	0.001034	21545.915	102783.4	32703.81	25695.85	15988.53	28779.35	111.52
1.5	100.2	150.3	20.8	23	23.4	27.4	24.6	19.1	20	1	0.016667	4	0.001029	5411.8102	23806.45	9411.853	9411.853	4876.02	7358.358	62.73
1.5	100.4	150.6	20	22	22.4	25.1	22.7	19	19.7	2	0.033333	4	0.001032	10798.23	62954.84	20984.95	18516.13	10320.47	17014.82	97.58
1.5	100.2	150.3	19.6	21	21.9	24.1	22	18.8	19.5	3	0.05	4	0.001036	16121.705	118040.3	37772.9	30462.02	17817.41	29510.08	146.37
1.5	100.1	150.2	19.6	21	21.8	23.5	21.5	18.9	19.3	4	0.066667	4	0.001034	21545.915	102783.4	31281.91	24809.79	15640.95	27672.46	111.52
1.5	100.7	151.1	20.9	24	23.7	27.9	24.4	18.8	20.3	1	0.016667	5	0.001036	5373.9018	32119.82	14052.42	13765.64	7412.265	12044.93	104.55
1.5	100.7	151.1	20.1	22	22.7	25.2	22.6	18.9	19.8	2	0.033333	5	0.001034	10772.958	67451.61	24527.86	21300.51	12847.93	21876.2	125.46
1.5	100.7	151.1	20.2	22	22.4	24.4	22	19	19.6	3	0.05	5	0.001032	16197.344	67451.61	27911.01	23806.45	14989.25	26980.65	125.46
1.5	100.5	150.8	19.7	21	21.9	23.8	21.6	18.9	19.4	4	0.066667	5	0.001034	21545.915	112419.4	37473.12	29978.49	18354.18	33309.44	139.4
1.5	101.1	151.7	20.7	23	23.5	28	24.7	18.7	20	1	0.016667	7	0.001039	5361.3834	29229.03	12437.89	12178.76	6285.813	9743.011	90.61
1.5	100.9	151.4	19.8	22	22.5	25.3	22.6	18.6	19.4	2	0.033333	7	0.001041	10697.846	59956.99	21802.54	18448.3	10738.57	17987.1	111.52
1.5	100.7	151.1	19.4	21	22	24.2	21.7	18.5	19.2	3	0.05	7	0.001044	16009.562	104924.7	34974.91	26980.65	16567.06	29510.08	146.37
1.5	100.7	151.1	19.2	21	21.5	23.5	21.2	18.4	19	4	0.066667	7	0.001046	21296.703	120967.7	40322.58	31217.48	18975.33	34562.21	150
1.5	100.2	150.3	20.4	23	23.6	28.5	25	18.2	19.5	1	0.016667	10	0.001051	5299.6563	26571.85	11691.61	10825.57	5675.54	8596.774	90.61
1.5	100.1	150.2	19.7	22	22.8	26.1	22.8	18.3	19.2	2	0.033333	10	0.001049	10623.776	57815.67	22483.87	17987.1	10377.17	17987.1	125.46
1.5	100.2	150.3	19.6	22	22.5	25	22.2	18.7	19.2	3	0.05	10	0.001039	16084.15	74946.24	23259.18	17750.42	10706.61	19271.89	104.55
1.5	100.7	151.1	19.2	21	21.9	24.2	21.6	18.4	19	4	0.066667	10	0.001046	21296.703	120967.7	37220.84	27649.77	16685.21	30241.94	150

10/26/96 rotons on Aluminum 0.150" Diameter Nozzle

Energy MeV	Current micro A	Power Watts	Temp (deg C) 1	2	3	4	5	Inlet	Outlet	Flow rate L / min	Mass flow kg / sec	Z / D	Viscosity	Reynold's Number	Calculated heat transfer coefficient by position 1	2	3	4	5	m c delta T
1.5	100.3	150.5	27	30	25.2	36.7	32.9	17.8	24.6	0.2	0.003333	1	0.001061	1050.2577	6647.405	5139.171	8264.342	3235.774	4050.075	94.792
1.5	100.2	150.3	19.4	22	19.6	27.1	23	15.1	18.2	0.4	0.006667	1	0.001135	1962.7264	12967.44	7853.521	12391.11	4646.667	7058.228	86.428
1.5	100.7	151.1	17.5	20	18.4	24.4	21.4	14.8	17.1	0.6	0.01	1	0.001144	2921.6962	22983.51	12411.1	17237.63	6464.113	9402.346	96.186
1.5	100.5	150.8	16.9	19	18	23.4	20.4	14.7	16.8	0.8	0.013333	1	0.001147	3885.7429	34339	17169.5	22892.67	8683.426	13253.65	117.096
1.5	101.4	152.1	16.4	19	17.7	22.7	19.8	14.6	16.5	1	0.016667	1	0.00115	4844.9259	47465.95	21907.36	27560.87	10547.99	16430.52	132.43

1/7/97	Target thickness (m)		Nozzle dia. (m)		Z/D	Target vol. cu.m										
16 mil		0.000406		0.022098		1	3.09E-07									
0.87" nozzle																
Flow Rate	Voltage	Current	Power	Front Temp	T_s	Jet Temp (T_f)	(T_s-T_f)	q"	q'''	Jet Velocity	Re	h	q" at rod	temp	k	temp	viscosity
GPM	V	A	W	C	C	C	C	W / m^2	W/m^3	m/s		W / m^2 K	W / m^2				
10	0.7	500	350	47.9	42.4	28.4	14.0	194638.123	1010343438	1.65	43786.106	13888.35	3433416	45.15724	15.21	28.4	0.00083
10	0.9	750	675	69.4	59.0	29.4	29.6	375373.523	1948519488	1.65	44646.555	12662.09	6621589	64.22273	15.54	29.4	0.000814
10	1	750	750	66.7	55.2	30.6	24.6	417081.693	2165021653	1.65	45724.812	16988.83	7357321	60.92518	15.48	30.6	0.000795
10	1	800	800	73.8	61.6	31.5	30.1	444887.139	2309356430	1.65	46568.313	14796.38	7847809	67.68365	15.59	31.5	0.000781
10	1.16	1000	1160	82.8	65.2	32	33.2	645086.351	3348566824	1.65	47050.512	19438	11379323	73.99343	15.70	32	0.000773
20	1.17	1000	1170	87.6	69.9	32.5	37.4	650647.441	3377433779	3.29	95085.601	17385.33	11477421	78.76254	15.78	32.5	0.000765
20	0.5	300	150	41.3	38.9	34.8	4.1	83416.3386	433004330.7	3.29	99893.447	20165.26	1471464	40.11832	15.13	34.8	0.000728
1/9,13/1997	Target thickness (m)		Nozzle dia. (m)		Z/D	Target vol. cu.m										
10 mil		0.000254		0.022098		1	1.93E-07									
0.87" nozzle																
Flow Rate	Voltage	Current	Power	Front Temp	T_s	Jet Temp (T_f)	(T_s-T_f)	q"	q'''	Jet Velocity	Re	h	q" at rod	temp	k	temp	viscosity
GPM	V	A	W	C	C	C	C	W / m^2	W/m^3	m/s		W / m^2 K	W / m^2				
9	0.45	350	157.5	26.7	25.4	17.2	8.2	133653.756	605201736.8	1.48	30490.31	16321.37	1545037	26.04444	14.89	17.2	0.001073
9	0.84	720	604.8	47	42.1	19.3	22.8	513230.424	2323974669	1.48	31794.075	22541.77	5932944	44.53399	15.20	19.3	0.001029
20	0.88	720	633.6	41.8	36.6	20	16.6	537669.968	2434640130	3.29	71628.03	32385.19	6215465	39.20117	15.11	20	0.001015
20	1.17	1000	1170	58.1	48.7	22.4	26.3	992856.475	4495784331	3.29	75339.327	37820.05	11477421	53.37606	15.35	22.4	0.000965
30	1.21	1000	1210	51.9	42.1	23.3	18.8	1026800.29	4649486359	4.94	115278.73	54737.61	11869811	46.97929	15.24	23.3	0.000946
35	1.21	1000	1210	52.7	42.9	25	17.9	1026800.29	4649486359	5.76	139658.93	57454.67	11869811	47.78574	15.26	25	0.000911
35	1.25	1000	1250	52.3	42.1	28.7	13.4	1060744.1	4803188388	5.76	152553.1	78924.89	12262202	47.21996	15.25	28.7	0.000834
35	1.44	1000	1440	33.5	21.5	13.2	8.3	1221977.2	5533273023	5.76	110059.94	146719.1	14126056	27.51434	14.91	13.2	0.001156
35	2.06	1500	3090	66.6	41.7	15.3	26.4	2622159.41	11873481694	5.76	114414.83	99459.31	30312163	54.13207	15.36	15.3	0.001112
37	1.8	1500	2700	77.5	56.0	30.3	25.7	2291207.25	10374886917	6.09	167914.52	89085.98	26486356	66.75953	15.58	30.3	0.000801
37	1.95	1500	2925	63.2	39.5	18.5	21.0	2482141.19	11239460827	6.09	128584.64	118005.9	28693552	51.36702	15.32	18.5	0.001046
37	2.28	1750	3990	79.2	47.3	20.8	26.5	3385895.16	15331777333	6.09	134769.07	127609.7	39140948	63.26661	15.52	20.8	0.000998
40	1.34	1000	1340	51.7	40.8	29.8	11.0	1137117.67	5149017952	6.58	179070.08	103429.9	13145080	46.24704	15.23	29.8	0.000812
40	1.85	1500	2775	78.1	56.0	31.9	24.1	2354851.9	10663078220	6.58	189329.3	97621.11	27222088	67.06118	15.58	31.9	0.000768
45	1.32	1000	1320	51.8	41.1	30.5	10.6	1120145.77	5072166937	7.40	205245.31	106105.9	12948885	46.42843	15.23	30.5	0.000797
50	2.04	1500	3060	66	41.3	24.3	17.0	2596701.55	11758205173	8.23	196280.91	152691.1	30017870	53.65312	15.36	24.3	0.000926
50	2.63	2000	5260	84.8	42.8	24.8	18.0	4463611.16	20211816735	8.23	198640.58	247741.6	51599345	63.8086	15.53	24.8	0.000915
50	2.84	2200	6248	94.4	44.9	26.2	18.7	5302023.3	24008256837	8.23	205142.35	284282.8	61291389	69.62526	15.63	26.2	0.000886

1/13/97	Target thickness (m)			Nozzle dia. (m)		Z/D	Target vol. cu.m										
10 mil		0.000254		0.022098		2	1.93E-07										
0.87" nozzle																	
Flow Rate	Voltage	Current	Power	Front Temp	T_s	Jet Temp (T_f)	(T_s-T_f)	q"	q'''	Jet Velocity	Re	h	q" at rod	temp	k	temp	viscosity
GPM	V	A	W	C	C	C	C	W / m^2	W/m^3	m/s		W / m^2 K	W / m^2				
10	0.6	500	300	38.9	36.4	27.8	8.6	254578.583	1152765213	1.65	43285.574	29485.28	2942928	37.66705	15.08	27.8	0.00084
10	1.35	1000	1350	74.9	64.2	28.3	35.9	1145603.63	5187443459	1.65	43701.882	31916.4	13243178	69.54694	15.63	28.3	0.000832
10	1.71	1250	2137.5	97.9	81.3	28.9	52.4	1813872.41	8213452143	1.65	44212.145	34609.58	20968365	89.60477	15.97	28.9	0.000822
20	0.63	500	315	37.3	34.7	30	4.7	267307.513	1210403474	3.29	90358.502	56785.05	3090075	36.00368	15.06	30	0.000805
20	1.34	1000	1340	81.2	50.4	30.6	19.8	1137117.67	5149017952	3.29	91449.623	57408.52	13145080	55.80374	15.39	30.6	0.000795
20	1.78	1250	2225	91.5	74.1	31.3	42.8	1888124.49	8549675330	3.29	92756.38	44115.41	21826719	82.79983	15.85	31.3	0.000784
20	2.1	1500	3150	102.1	77.7	32.2	45.5	2673075.13	12104034737	3.29	94492.397	58812.36	30900748	89.87546	15.97	32.2	0.000769
20	2.34	1750	4095	104.7	72.9	33.3	39.6	3474997.66	15735245158	3.29	96704.51	87804.95	40170973	88.78816	15.95	33.3	0.000752
	2.5	2000	5000														
1/14/97	Target thickness (m)			Nozzle dia. (m)		Z/D	Target vol. cu.m										
16 mil		0.000406		0.022098		2	3.09E-07										
0.87" nozzle																	
Flow Rate	Voltage	Current	Power	Front Temp	T_s	Jet Temp (T_f)	(T_s-T_f)	q"	q'''	Jet Velocity	Re	h	q" at rod	temp	k	temp	viscosity
GPM	V	A	W	C	C	C	C	W / m^2	W/m^3	m/s		W / m^2 K	W / m^2				
20	0.46	500	230	36	33.8	14.6	19.2	391709.223	405034463.3	3.29	62550.504	20426.98	2256245	34.88803	15.04	14.6	0.001162
20	0.73	750	547.5	47.6	42.4	15.4	27.0	932438.259	964158124.6	3.29	63547.76	34579.26	5370844	44.98262	15.21	15.4	0.001144
30	0.46	500	230	31.6	29.4	16.2	13.2	391709.223	405034463.3	4.94	96865.996	29755.7	2256245	30.48209	14.96	16.2	0.001126
30	0.74	750	555	45.3	40.0	17.6	22.4	945211.386	977365770.1	4.94	99692.546	42235.51	5444418	42.63977	15.17	17.6	0.001094
70	0.46	500	230	29.7	27.5	19.2	8.3	391709.223	405034463.3	11.52	240640.97	47424.25	2256245	28.57984	14.93	19.2	0.001057
70	0.69	750	517.5	43.6	38.6	19.9	18.7	881345.752	911327542.4	11.52	244328.71	47057.3	5076552	41.1146	15.14	19.9	0.001041
70	0.98	1000	980	65.8	56.6	20.3	36.3	1669021.91	1725799018	11.52	246487.18	45986.86	9613566	61.19673	15.48	20.3	0.001032
70	1.2	1250	1500	82.6	68.7	20.8	47.9	2554625.37	2641529108	11.52	249239.5	53296.52	14714642	75.66616	15.73	20.8	0.001021
100	0.47	500	235	27.8	25.5	22.8	2.7	400224.641	413839560.3	16.45	372703.11	147882.4	2305294	26.65319	14.90	22.8	0.000975
100	0.73	750	547.5	36.6	31.3	23.3	8.0	932438.259	964158124.6	16.45	377110.87	116569	5370844	33.94951	15.02	23.3	0.000964
100	1.02	1000	1020	53.3	43.6	24.2	19.4	1737145.25	1796239794	16.45	385313.28	89608.71	10005957	48.44295	15.27	24.2	0.000943
100	1.26	1250	1575	65.8	51.0	24.6	26.4	2682356.64	2773605564	16.45	389074.44	101737.6	15450374	58.38272	15.44	24.6	0.000934
80	0.92	1000	920	66.8	58.2	26.6	31.6	1566836.89	1620137853	13.16	327230.56	49624.53	9024981	62.48692	15.51	26.6	0.000889
90	0.95	1000	950	62.6	53.6	27.1	26.5	1617929.4	1672968435	14.81	372918.07	60947.3	9319273	58.12318	15.43	27.1	0.000877
100	0.99	1000	990	60.6	51.2	27.6	23.6	1686052.74	1743409212	16.45	419808.58	71306.58	9711664	55.92256	15.39	27.6	0.000866
117	1	1000	1000	59.9	50.4	28.9	21.5	1703083.58	1761019406	19.25	508585.05	79049.63	9809761	55.17224	15.38	28.9	0.000836
120	1.05	1000	1050	58.6	48.7	29.5	19.2	1788237.76	1849070376	19.74	530300.64	93337.76	10300249	53.62939	15.36	29.5	0.000823

1/14/97	Target thickness (m)			Nozzle dia. (m)		Z/D	Target vol. cu.m										
16 mil		0.000406		0.017018		1	3.09E-07										
0.67" nozzle																	
Flow Rate	Voltage	Current	Power	Front Temp	T_s	Jet Temp (T_f)	(T_s-T_f)	q"	q'''	Jet Velocity	Re	h	q" at rod	temp	k	temp	viscosity
GPM	V	A	W	C	C	C	C	W / m^2	W/m^3	m/s		W / m^2 K	W / m^2				
20	0.93	750	697.5	51.9	45.3	20.9	24.36	1187900.8	1228311035	5.55	123964.28	48769.87	6842309	48.57863	15.27	20.9	0.000989
30	0.89	750	667.5	44.8	38.4	22.6	15.79	1136808.29	1175480453	8.32	193428.28	71983.49	6548016	41.59631	15.15	22.6	0.000951
35	0.9	750	675	44	37.5	23.3	14.22	1149581.42	1188688099	9.71	229468.17	80863.32	6621589	40.75818	15.14	23.3	0.000935
50	0.96	750	720	42.4	35.5	24.2	11.27	1226220.18	1267933972	13.87	335069.49	108800.3	7063028	38.93519	15.11	24.2	0.000915
60	0.95	750	712.5	42.1	35.2	24.8	10.44	1213447.05	1254726327	16.64	408107.11	116252.6	6989455	38.66901	15.10	24.8	0.000901
70	0.96	750	720	41.6	34.7	26	8.66	1226220.18	1267933972	19.42	490831.53	141576.4	7063028	38.1306	15.09	26	0.000874
77	0.97	750	727.5	41.3	34.3	26.6	7.69	1238993.3	1281141618	21.36	548383.93	161140.2	7136601	37.79446	15.09	26.6	0.000861
1/14/97	Target thickness (m)			Nozzle dia. (m)		Z/D	Target vol. cu.m										
16 mil		0.000406		0.017018		2	3.09E-07										
0.67" nozzle																	
Flow Rate	Voltage	Current	Power	Front Temp	T_s	Jet Temp (T_f)	(T_s-T_f)	q"	q'''	Jet Velocity	Re	h	q" at rod	temp	k	temp	viscosity
GPM	V	A	W	C	C	C	C	W / m^2	W/m^3	m/s		W / m^2 K	W / m^2				
80	0.97	750	727.5	39.3	32.3	27.2	5.1	1238993.3	1281141618	22.19	577564.49	244363.9	7136601	35.78514	15.05	27.2	0.000849
85	0.97	750	727.5	38.9	31.9	27.7	4.2	1238993.3	1281141618	23.58	619942.16	297100.8	7136601	35.38514	15.05	27.7	0.00084
87	0.75	500	375	29.7	26.0	28.5	-2.5	638656.342	660382277.1	24.13	645091.47	-260130	3678661	27.87243	14.92	28.5	0.000827
87	0.98	750	735	36	28.9	28.6	0.3	1251766.43	1294349263	24.13	646436.55	4646831	7210175	32.43469	14.99	28.6	0.000825
87	1.24	1000	1240	46.9	35.0	29	6.0	2111823.64	2183664063	24.13	651873.44	352599.5	12164104	40.94465	15.14	29	0.000818
87	1.4	1250	1750	56	39.3	29.1	10.2	2980396.26	3081783960	24.13	653246.98	291858.4	17167082	47.6559	15.25	29.1	0.000816
87	1.6	1500	2400	71	48.4	29.4	19.0	4087400.59	4226446574	24.13	657402.55	214852.8	23543427	59.7121	15.46	29.4	0.000811
87	1.78	1750	3115	89.2	60.4	29.6	30.8	5305105.35	5485575449	24.13	660202.44	172440.9	30557407	74.78239	15.71	29.6	0.000808
1/16/97	Target thickness (m)			Nozzle dia. (m)		Z/D	Target vol. cu.m										
16 mil		0.000406		0.017018		2	3.09E-07										
0.67" nozzle																	
Flow Rate	Voltage	Current	Power	Front Temp	T_s	Jet Temp (T_f)	(T_s-T_f)	q"	q'''	Jet Velocity	Re	h	q" at rod	temp	k	temp	viscosity
GPM	V	A	W	C	C	C	C	W / m^2	W/m^3	m/s		W / m^2 K	W / m^2				
87	0.74	500	370	25.8	23.4	15.8	7.57	1120250.53	437466652.2	24.13	510253.49	148007.1	3629612	24.58445	14.86	15.8	0.001045
87	0.95	750	712.5	34.2	29.6	16	13.56	2157239.2	842418891	24.13	511938.62	159099.2	6989455	31.87954	14.99	16	0.001042
87	1.16	1000	1160	45.4	37.9	16.3	21.62	3512136.8	1371517072	24.13	514487.3	162418	11379323	41.66203	15.15	16.3	0.001036
87	1.37	1250	1712.5	59.2	48.3	16.5	31.81	5184943.34	2024761194	24.13	516200.57	162975.7	16799216	53.7571	15.36	16.5	0.001033
87	1.53	1500	2295	68.3	53.8	16.9	36.92	6948581	2713475586	24.13	519661.56	188183.3	22513402	61.06227	15.48	16.9	0.001026
87	1.71	1750	2992.5	69.1	50.2	17.9	32.30	9060404.64	3538159342	24.13	528520.53	280501.6	29355711	59.65036	15.46	17.9	0.001009
87	1.92	2000	3840	82.5	58.5	18.4	40.13	11626383.9	4540194444	24.13	533064.27	289736.8	37669484	70.5137	15.64	18.4	0.001
87	2.1	2250	4725	103.1	74.2	18.8	55.38	14305902.1	5586567382	24.13	536755.89	258342.3	46351123	88.63789	15.95	18.8	0.000993
87	2.2	2350	5170	112.3	80.9	20.4	60.53	15653230.4	6112709707	24.13	552048.27	258615.4	50716467	96.61353	16.09	20.4	0.000966

REFERENCES

1. Shefer, R.E., Klinkowstein, R.E., and Yanch, J.C., "A High Current Electrostatic Accelerator for Boron Neutron Capture Therapy," in *Proceedings of the 5th International Conference on Applications of Nuclear Techniques,* Crete, 1996.

2. Howard, W.B., "Accelerator Based Boron Neutron Capture Therapy," MIT Ph.D. Thesis. 1997.

3. Shefer, R. E., Klinkowstein, R. E., Yanch, J. C., and Howard, W. B., "Tandem Electrostatic Accelerators for Boron Neutron Capture Therapy," in *Proceedings of the 1rst International Workshop on Accelerator Based Neutron Sources for BNCT,* Jackson, WY., 1994.

4. Hiskes, J. R., Karo, A. M., Bacal, M., Bruneteau, A. M., and Graham, W. G., "Hydrogen Vibrational Population Distributions and Negative Ion Concentrations in a Medium Density Hydrogen Discharge," *Journal of Applied Physics,* **53**, 3469-3475 (1982).

5. Bacal, M., Bruneteau, A. M., Graham, W. G., Hamilton, G. W., and Nachman, M., "Pressure and Electron Temperature Dependence of H^- density in a Hydrogen Plasma," *Journal of Applied Physics* **52**, 1247-1254 (1981).

6. Holmes, A. J. T., Dammertz, G., and Green, T. S., "H^- and Electron Production in a Magnetic Multipole Source," *Journal of Applied Physics,* **56**, (1985).

7. Yanch, J. C., Zhou, X. L., Shefer, R. E., and Klinkowstein, R. E., "Accelerator- Based Epithermal Neutron Beam Design for Neutron Capture Therapy," *Medical Physics,* **19**, 709-721 (1992).

8. Scoles, G. J., *Handbook of Rectifier Circuits*, New York: John Wiley & Sons.

9. Incropera, F. P., and DeWitt, D. P, *Fundamentals of Heat and Mass Transfer*, New York: John Wiley & Sons, 1990.

10. Pais, M. R., and Leland, J. E., and Chang, W. S., and Chow, L.C, "Single-Phase Heat Transfer Characteristics of Submerged Jet Impingement Cooling Using JP-5," in *Proceedings of the Conference on Thermal Phenomena in Electronic Systems,* 1994, pp. 178-183.

11. Lienhard, J.H., an Eichhorn, R. "Peak Boiling Heat Flux on Cylinders in a Cross Flow," *International Journal of Heat and Mass Transfer*, **86**, 1135 (1976).

12. Lide, D.R editor. *CRC Handbook of Chemistry and Physics 75th ed.*, Boca Raton: CRC Press, 1995.

13. Stonehouse, A.J, and Marder, J.M., *ASM Handbook 10th ed.*, ASM International, 1990.

14. Schyler, D. J., Ferrieri, R. A., Firouzbakht, M. L., and Garcia, I., "Correlation of Hole Size in Support Windows with Calculated Yield Strengths," in *Proceedings of the 14th International Conference on the Application of Accelerators in Research and Industry*, Denton, Tx. 1996.

15. Maceika, A. A., and Skema, R. K., *Heat Transfer-Soviet Research,* **22**, 587-594 (1990).

16. Rice, R. A., and Garimella, S.V., "Heat Transfer from Discrete Heat Sources Using an Axisymmetric, Submerged and Confined Liquid Jet," in *Proceedings of the 10th International Heat Transfer Conference*, 1994, pp. 89-94.

17. Rice, R. A., and Garimella, S.V., "Confined and Submerged Liquid Jet Impingement Heat Transfer," *Journal of Heat Transfer,* **117,** 871-877 (1995).

18. Song, H., Yanch, J.C, and Klinkowstein, R.E., "An Accelerator-Based Neutron Source for Fast Neutron Brachytherapy," in *Proceedings of the 14th International Conference on the Application of Accelerators in Research and Industry*, Denton, Tx. 1996.

19. Hammitt, F. G., and Heymann, F. J., "Liquid-Erosion Failures," *ASM Handbook* **2**, 163-171 (1986).

Other References

Beitz, W. ed., and Kuttner, K. H. ed., *Dubbel Handbook of Mechanical Engineering*, London: Springer-Verlay, (1994).

Cleland, M. R., Seiler, R. F., and Wegner, H. E., "High Current Target for Positive Ion Accelerators," *IEEE Transactions on Nuclear Science*, **June**, 943-944 (1967).

Gabour, L. A., and Lienhard, J. H., "Wall Roughness Effects on Stagnation-Point Heat Transfer Beneath an Impinging Liquid Jet," *Journal of Heat Transfer,* **116**, 81-87 (1994).

Hanley, P. R., Haberl, A. W., and Taylor, A., "Water Cooled Targets for Intense Ion Beams," *IEEE Transactions on Nuclear Science* , **June**, 933-937 (1967).

Howard, W. B. and Yanch, J. C., "Shielding Design and Dose Assessment for Accelerator Based Neutron Capture Therapy," *Health Physics* 68, 723-730 (1995).

Scharf, W., *Particle Accelerators and Their Uses*, New York: Harwood Academic Publishers, (1986).

Steidel, R. F., *Marks' Standard Handbook for Mechanical Engineers, 9th Ed.*, New York: McGraw-Hill Book Company, (1987).

Van de Graff, R. J., "Tandem Electrostatic Accelerators," *Nuclear Instruments and Methods*, **8**, 195-202 (1959).